15-year variability of desert dust optical depth on global and regional scales

Stavros-Andreas Logothetis[1], Vasileios Salamalikis[1], Antonis Gkikas[2] Stelios Kazadzis[3,4], Vassilis Amiridis[2] and Andreas Kazantzidis[1]

[1]Laboratory of Atmospheric Physics, Department of Physics, University of Patras, 26500 Patras, Greece
[2]Institute for Astronomy, Astrophysics, Space Applications and Remote Sensing, National Observatory of Athens, Athens, 15236, Greece
[3]Physics - Meteorology Observatory Davos, Word Radiation Center, Switzerland
[4]Institute of Environmental Research and Sustainable Development, National Observatory of Athens, Greece

Correspondence to: Andreas Kazantzidis (akaza@upatras.gr)

Abstract. This study aims to investigate the global, regional and seasonal temporal dust changes as well as the effect of dust particles on total aerosol loading, using the Modis Dust AeroSol (MIDAS) fine resolution dataset. MIDAS delivers dust optical depth (DOD) at fine spatial resolution (0.1° x 0.1°) spanning from 2003 to 2017. Within this study period, the dust burden has been increased across Central Sahara (up to 0.023 yr^{-1}) and Arabian Peninsula (up to 0.024 yr^{-1}). Both regions observed their highest seasonal trends in summer (up to 0.031 yr^{-1}). On the other side, declining DOD trends are encountered in Western (down to −0.015 yr^{-1}) and Eastern (down to −0.023 yr^{-1}) Sahara, Bodélé Depression (down to −0.021 yr^{-1}), Thar (down to −0.017 yr^{-1}) and Gobi (down to −0.011 yr^{-1}) Deserts and Mediterranean Basin (down to −0.009 yr^{-1}). At spring, the most negative seasonal trends are recorded in Bodélé Depression (down to −0.038 yr^{-1}) and Gobi Desert (down to −0.023 yr^{-1}) whereas in West (down to −0.028 yr^{-1}) and East Sahara (down to −0.020 yr^{-1}), and Thar Desert (down to −0.047 yr^{-1}) at summer. Over western and eastern sector of Mediterranean Basin, the most negative seasonal trends are computed at summer (down to −0.010 yr^{-1}) and spring (down to −0.006 yr^{-1}), respectively. The effect of DOD on the total aerosol optical depth (AOD) change is determined by calculating the DOD to AOD trends ratio. Over Sahara Desert the median ratio values range from 0.83 to 0.95 whereas in other dust affected areas (Arabian Peninsula, South Mediterranean, Thar and Gobi Deserts) the ratio value is approximately 0.6. In addition, a comprehensive analysis of the factors effecting the sign, the magnitude and the statistical significance of the calculated trends is conducted. Firstly, the implications between the implementation of geometric mean instead of arithmetic mean to trend calculations are discussed revealing that the arithmetic-based trends tend to overestimate compared with the geometric-based trends both over land and ocean. Secondly, an analysis interpreting the differences in trend calculations under different spatial resolutions (fine and coarse) and time intervals is conducted.

1 Introduction

Dust particles emitted from natural or anthropogenic sources are a major contributor to the atmospheric aerosol burden in terms of mass (Zender et al. 2004; Textor et al., 2006; Kok et al., 2017). Among aerosol properties, AOD describes adequately aerosols' load, in optical terms, corresponding to the entire atmospheric column. The proportion of AOD attributed to dust particles consists the DOD. The spatiotemporal patterns of mineral particles are determined by the dust life cycle components, characterized by a pronounced heterogeneity (Mahowald et al., 2014). The main natural dust sources are located in the northern hemisphere (Goudie and Middleton., 2006), with Sahara region being the most dominant one (Prospero et al., 2002; Goudie and Middleton, 2006; Rajot et al., 2008; Alizadeh-Choobari et al., 2014a). Other active source areas of mineral particles are situated in the Middle East and the region stretching from Mesopotamia to the Oman coasts in south Arabian Peninsula (Prospero et al., 2002; Ginoux et al., 2012), in southwest Asia and Sistan Basin (Iran-Pakistan-Afghanistan) (Alizadeh-Choobari et al., 2014b; Rashki et al., 2015), in Central Asia across the Karakum (Turkmenistan-Uzbekinstan) and Kyzylkum Deserts (southeast of the Aral sea in Uzbekistan) (Elguindi et al., 2016), in East Asia with Taklamakan (Tarim basin in northwest China) and Gobi (north China – south Mongolia) deserts (Ginoux et al., 2012), and in North America with Black Rock and Smoke, Great Salt Lake, and Chihuahuan and Sononan deserts (Ginoux et al., 2012).

Mineral dust aerosols are uplifted, accumulated into the atmosphere, and transported over enormous distances (up to some thousands of kilometers) from their sources (Goudie and Middleton., 2006) driven by the prevailing winds. Schepanski et al. (2018) reported that the transport distance of dust particles is strongly related to their residence time, which is analogous to the dust lifetime, dust layer altitude, atmospheric circulation pattern, buoyancy and gravitational forces. van der Does et al. (2018) also denoted that strong winds, turbulence, electrostatic forces developed by dust particles' charging, and thunderstorms or tropical cyclones may potentially enhance the residence time of dust aerosols into the atmosphere. On a seasonal basis, dust particles can be transported from north Africa towards the Atlantic Ocean reaching Caribbean, Central America, southern United States (in boreal summer) and South America (in spring and winter) (Griffin et al., 2002; Prospero and Lamb., 2003; Kalashnikova et al., 2008; Huang et al., 2010; Tsamalis et al., 2013; Prospero and Mayol-Bracero., 2013). Additionally, Saharan dust is advected towards the Mediterranean and Europe (Mona et al., 2006; 2012, Papayannis et al., 2008; Basart et al., 2009; Schepanski et al., 2018; Gkikas et al. 2015; 2016, Logothetis et al., 2020, 2021).

During the last decades, numerous studies have been conducted using observations from various satellite sensors. Prospero et al. (2002) and Ginoux et al. (2012) identified the global dust sources relying on Total Ozone Mapping Spectrometer (TOMS, Torres et al., 2002) and Moderate Resolution Imaging Spectroradiometer (MODIS, Remer et al., 2008), respectively. More specifically, the studies of Prospero et al. (2002) and Ginoux et al. (2012) were based on the frequency of occurrence (FoO) of TOMS absorbing aerosol index (AAI) and MODIS-based DOD, respectively, exceeding defined thresholds. In addition, Ginoux et al. (2012) associated the dust frequency with three clusters such as hydrologic and non-hydrologic natural or anthropogenic in order to distinguish the dust origin. Similarly, at a regional scale, Schepanski et al. (2012) implemented a comprehensive analysis on the potential differences of Saharan dust active sources within the intercomparison of aerosol

properties observations derived from MODIS, Meteosat Second Generation (MSG) and Ozone Monitoring Instruments (OMI). Voss and Evan (2020) presented a global DOD climatology, both over land and ocean, using MODIS (Aqua and Terra) from 2001 to 2018 and Advanced Very High Resolution Radiometer (AVHRR) over ocean from 1981 to 2018. Similarly, Clarisse et al. (2019) performed a global seasonal DOD climatology relying on Infrared Atmospheric Sounding Interferometer (IASI) retrievals, during the 2008−2017. Yu et al. (2019), derived DOD using MODIS, IASI and Multiangle Imaging Spectroradiometer (MISR) and in conjunction with dust vertical profiles from Cloud−Aerosol Lidar with Orthogonal Polarization (CALIOP) (Shikwambana and Sivakumar., 2018) investigated the dust deposition and loss frequency across the Tropical Atlantic Ocean on a seasonal basis.

The investigation of dust loads' variation at interannual time scales is quite critical for assessing the associated impacts on climate as well as the response of these tendencies to environmental factors. Since the majority of remote sensing instruments provide an AOD product, numerous studies on a global scale, are focused on the estimation of AOD temporal trends, which are not always representative of DOD, being mixed with other aerosol types (Zhang and Reid, 2010; de Meij et al., 2012; Hsu et al., 2012; Yoon et al., 2014; Pozzer et al., 2015; Alfaro-Contreras et al., 2017; Zhao et al., 2017; Che et al., 2019) and regional scales (Guo et al., 2011; Li, 2014; Klingmüller et al., 2016; Floutsi et al., 2016; Dahutia et al., 2017; Hu et al., 2018; Zhang et al., 2018). Limited satellite studies are dedicated to the estimation of DOD temporal trends due to the deficiency to quantify accurately the portion of AOD attributed to DOD. Prior studies have investigated the interannual patterns of DOD over the "dusty" regions of the planet. Dust load has been increased across the Sahara Desert, based on MODIS-Aqua derived DOD dataset during 2003−2018 (Voss and Evan 2020). Notaro et al. (2015) detected a regime shift in dust activity between 1998−2005 (inactive dust period) and 2007−2013 (active dust period) across Arabian Peninsula, which is attributed to the prolonged drought along the Fertile Crescent. Through the synergy of MISR DODs and back trajectories, they revealed that the positive DOD anomalies (increased dust burden) are strongly connected with dust advection from the Fertile Crescent towards the Arabian Peninsula. These findings are consistent with the strong positive AOD (Klingmüller et al., 2016) and DOD (Voss and Evan 2020) trends reported in the area. Voss and Evan (2020), found a reduction of dust load across the Northern African coasts over the period 2001−2018, based on MODIS-Terra DOD dataset. Declining DOD trends have also been reported in Central Asia by Xi and Sokolik (2015), who analyzed MODIS and Sea-viewing Wide Field-of-view Sensor (SeaWiFs) DODs for a 15-year period (2000-2014). DOD trend sign is also abruptly changed from positive (1999-2009) to negative (2010−2016) over East Asia and North Pacific Ocean in springtime, based on Modern-Era Retrospective Analysis for Research and Applications, Version 2 (MERRA-2) (Gelaro et al., 2017) measurements (Guo et al., 2019). Across South Asia, a negative shift in DOD interannual variation is recorded during the pre-monsoon season between 2008–2012 and 2013–2017, based on CALIOP observations (Lakshmi et al., 2019). In the southern sector of the Gobi Desert, declining DOD trends are observed from MODIS and CALIOP DOD datasets during 2007−2019 (Song et al., 2021).

This study's main objective is to investigate the dust temporal variations at global, regional, and seasonal scales, using the newly MIDAS DOD product from 2003–2017. A few aspects regarding the innovative points of this research are highlighted below to support the scientific contribution to the relevant research field. First, in contrast to the existing studies, this trend

97 analysis relies on fine spatial resolution data, making it feasible to depict in detail the spatial patterns of the DOD variations.

98 Such information can be critical for interpreting the perturbations of the radiation fields, environmental impacts, and health

99 effects attributed to dust particles. One more advantage of the high resolution DOD analysis is the flexibility of the final grid

100 size selection depending on data availability, which is a critical aspect when satellite observations are used. MIDAS data can

101 be easily upscaled at coarser spatial resolutions in order to match spaceborne observations, which have been commonly used

102 in other trend analyses available in the literature (Hsu et al., 2012; Yoon et al., 2014; Notaro et al., 2015; Pozzer et al., 2015;

103 Klingmüller et al., 2016; Alfaro-Contreras et al., 2017; Che et al., 2019; Guo et al., 2019; Voss and Evan 2020; Song et al.,

104 2021). In addition, fine spatial resolution data ensure a more realistic collocation with ground-based measurements for

105 validating the obtained DOD trends. Second, quite a few studies concentrate on pure DOD (Xi and Sokolik 2015; Guo et al.,

106 2019; Lakshmi et al., 2019; Voss and Evan 2020; Song et al., 2021) rather than AOD to analyze the trends of mineral particles'

107 load. Even though the consideration of the latter parameter is quite reasonable across deserts, its representativeness over

108 downwind areas is questionable due to the coexistence of other aerosol types. Such types can also affect the DOD trend

109 uncertainty. In MIDAS, this issue is addressed by the adjustment of MODIS AOD to DOD in terms of the MERRA-2 dust

110 fraction, while in other studies, aerosol size and natural optical properties, which their quality above land is downgraded, are

111 used in parallel. Third, taking advantage that MIDAS provides DOD and quality assured AOD, their trends are discussed

112 jointly for assessing the contribution of dust burden temporal variations to those of the total aerosol load. It should be mentioned

113 that this is the first study assessing the effect of DOD to total AOD trends across the major desert dust areas of the planet,

114 highlighting the potential role of desert dust particles in past, present, and future AOD trend studies. Fourth, the investigation

115 of the potential impact on trends' magnitude, sign, and statistical significance when different DOD aggregations (i.e. arithmetic

116 mean vs. geometric mean) are considered among various spatial and temporal scales. Fifth, the DOD interannual variations

117 are discussed for the entire study period on a seasonal basis and sub-periods for detecting alternations on DOD trends within

118 the period of interest.

119   The current paper is organized as follows. Sect. 2 describes the (i) MIDAS (Sect. 2.1) and (ii) AERONET (Sect. 2.2)

120 datasets as well as the trend detection methodology (Sect. 2.3). The results section (Sect. 3) is divided into three sub-sections

121 analyzing (i) the global AOD and DOD tendencies (3.1), along with the sensitivity analyses between arithmetic and geometric

122 means (3.1.1), fine (0.1° x 0.1°) and coarse (1° x 1°) spatial resolutions (Sect. 3.1.2), MIDAS DOD and AEROENT retrievals

123 (Sect. 3.1.3), and filtered and non-filtered data trend calculations (Sect. 3.1.4), (ii) global dust temporal trends on a seasonal

124 basis (Sect. 3.2), and (iii) DOD temporal tendencies into specific regions (Sect. 3.3). Finally, a discussion focusing on the main

125 findings of this study is presented in the summary and conclusion section (Sect. 4). The current study represents a practical

126 implementation of the MIDAS dataset and aims to demonstrate its feasibility on the estimation of dust load variation at various

127 temporal and spatial scales.

2 Data and Methods

2.1 Modis Dust AeroSol (MIDAS) dataset

MIDAS dataset (Gkikas et al., 2021a) provides columnar DOD at 550 nm, on a daily basis over the 15-year period spanning from 2003 to 2017, at a global scale and fine spatial resolution (0.1° x 0.1°). Its development has relied on the synergistic implementation of quality filtered AOD retrievals from MODIS-Aqua (Level 2; Collection 6.1) and MERRA-2 dust fraction (MDF), both reported at 550 nm. More specifically, the multiplication of MODIS-Aqua AOD with MDF provides the MIDAS-DOD on MODIS native grid which is converted to an equidistant lat-lon projection. In order to justify the reliability of MDF, it has been evaluated against the corresponding portion provided by the LIVAS database (Amiridis et al., 2013; 2015). Based on the aforementioned assessment analysis, it has been revealed an adequate representation of MERRA-2 dust fraction, in optical terms, over the main dust sources and the outflow regions, in contrast to areas where dust presence is weak. Therefore, the combination of highly accurate MODIS AODs (Wei et al., 2019b) and quite reliable MDF results in a trustworthy MIDAS DOD product as it has been justified via its evaluation against AERONET dust-like AOD and its intercomparison versus DOD derived by LIVAS and MERRA-2. For the former analysis, the ground-based AODs have been treated appropriately in order to resemble DOD, as much as possible, assuming that the contribution of fine mineral particles is negligible and trying to minimize the contribution of non-dust aerosol species to the columnar aerosol load. Under these assumptions, the evaluation metrics, both at global and station level, reveal a quite high level of agreement between the two datasets. At global scale, there is a high level of agreement between MIDAS and AERONET DODs as indicated by the high correlation (~0.9) and the low positive bias (0.004 or 2.7%). Across the 'dust belt', the correlation coefficients can reach up to 0.98 at station level whereas positive biases (mostly lower than 0.06) are found. Outside of this zone, the correlation reduces, and the biases of similar magnitude are switching to negative. Likewise, it has been evident a considerable consistency among MIDAS, LIVAS and MERRA-2 DODs at global and hemispherical scales, despite the different approaches applied for the DOD derivation, whereas the intercomparison results are regionally dependent. Summarizing, the reliability of the MIDAS DOD justified in Gkikas et al. (2021a) strengthens its applicability for investigating the temporal trends of dust aerosol burden over long-time periods and at various spatial scales.

2.2 AERONET

On a regional basis, the reliability of MIDAS DOD trends has been evaluated using ground-based measurements from AERONET (Holben et al., 1998). AERONET provides information for the spectral columnar AOD using direct spectral solar irradiance. In addition, the physical and optical properties of aerosols can be derived by applying the Dubovik and King (2000) inversion algorithm. DOD ground-based measurements can be approached using AERONET retrievals, however, an aerosol classification scheme is mandatory. Through MIDAS evaluation procedure, the discrimination of dust load from non-dust aerosol species has been performed in terms of the Ångström wavelength exponent at 440-870 nm ($AE_{440-870\ nm}$) and the

160   difference between single scattering albedo at 440 nm (SSA$_{440\ nm}$) and 675 nm (SSA$_{675\ nm}$). AE$_{440-870\ nm}$ has been used as an

161   indicator of particles size (coarse or fine aerosols) in numerous aerosol classification studies (Basart et al., 2009; Mielonen et

162   al., 2009; Lee et al., 2010; Giles et al., 2012; Hamill et al., 2016; Zheng et al., 2017; Che et al., 2018; Logothetis et al., 2020).

163   In addition, the aerosols origin can be acquired using either the difference between SSA at different wavelengths or specific

164   spectral SSA thresholds. In Gkikas et al. (2021a), the pure dust conditions have been succeeded using a very restricted threshold

165   limit of AE$_{440-870}$ nm (≤ 0.75) along with a positive difference of SSA$_{675\ nm}$ − SSA$_{440\ nm}$. Despite the favorable dust conditions

166   retrieved through the SSA retrievals, the data availability strongly decreases causing difficulties in trend calculations. In the

167   current study, the evaluation of MIDAS DOD trends is performed by using the AERONET coarse mode AOD at 500 nm,

168   derived from the spectral deconvolution algorithm (SDA) (O'Neill et al., 2001, 2003). The performance of the SDA algorithm,

169   in terms of segregating the fine and coarse aerosol modes, has been justified against ground-based observations (Kaku et al.,

170   2014). Only quality assured data (cloud-screened), including pre-field and post-field calibrations (Level 2.0, L2) from

171   AERONET Version 3 (V3) (Giles et al., 2019) are used. It should be mentioned that cAOD does not represent profoundly the

172   dust load due to the presence of sea-salt particles.

173

2.3 Temporal trends methodology

175   The spatiotemporal changes of dust particles' burden, over the period 2003 – 2017, are investigated by calculating the

176   annual trends derived by the monthly MIDAS DODs. At each grid-cell, the monthly DOD averages are calculated when the

177   20% (≥ 6 days) of daily data are available (Hsu et al., 2012). Subsequently, at the grid points with more than 60 months

178   available (5 out of 15 complete years) linear trends are calculated by the implementation of the following equation,

179   $$Y_t = \mu + S_t + \omega X_t + N_t \tag{1}$$

180   where Y$_t$ is the monthly averaged values, μ the offset term, S$_t$ is the seasonal term (i.e. long-term monthly value), ω the linear

181   trend and N$_t$ the residuals. The seasonality is removed by subtracting S$_t$ from Y$_t$. The statistical significance of ω is derived

182   according to Weatherhead et al. (1998). N$_t$ follows a 1st-order autoregressive process (significant lag-1 autocorrelation),

183   $$N_t = \varphi N_{t-1} + \varepsilon_t \tag{2}$$

184   with ε$_t$ is the white noise and φ the lag-1 autocorrelation coefficient. The standard deviation of the trend can be expressed as,

185   $$\sigma_\omega \approx \frac{\sigma_N}{n^{3/2}} \sqrt{\frac{1+\varphi}{1-\varphi}} \tag{3}$$

186   where σ$_N$ is the standard deviation of N$_t$ and n is the number of complete years depending on the data availability at each grid

187   cell without always considering the entire period (i.e. a constant value of 15 years). When |ω/σ$_\omega$|>2, significant temporal trends

188   are considered at a 95% confidence level. The methodology of Weatherhead et al. (1998) is commonly applied in numerous

189   studies concerning the detection of temporal trends in AOD (Hsu et al., 2012; Babu et al., 2013; Li et al., 2014; Kumar et al.,

190 2015, 2018; Pozzer et al., 2015; Adesina et al., 2016; Alfaro-Contreras et al., 2017; Zhang et al., 2018; Ningombam et al.,
191 2019). Additionally, for comparison purposes with previous studies, AOD and DOD linear trends are calculated also at 1°
192 spatial resolution. The re-gridding procedure from fine to coarse spatial resolution is implemented following Levy et al. (2009)
193 (upper branch in Fig. 5 of their publication). For the calculation of regional trends (Sect. 3.3), the same approach is adopted.
194 First, daily spatial grids of 0.1° are temporally averaged to create monthly data. Then, monthly grids with 1° spatial resolutions
195 are generated using a weighted aggregation of monthly fine grids. The weighting factors are defined in terms of latitude. More
196 specifically, this weighting scheme considers the fraction between the area covered by each fine grid-cell to the total available
197 surface area within the coarse grid-cell.

198   The appropriate selection of the statistical average metric (e.g. arithmetic or geometric mean) is reflected to the
199 background probability distribution which the raw data are resembled. For instance, the vast majority of the studies focusing
200 on AOD statistics have thoroughly consider that AOD follows a Gaussian distribution using the simple arithmetic mean for
201 temporal and spatial aggregations. Nevertheless, the frequency distribution of AOD follows is more well fitted to the log-
202 normal distribution (O' Neill et al., 2000). Sayer and Knobelspiesse (2019) designated that the calculation of the geometric
203 instead of the arithmetic mean for obtaining temporal and spatial AOD trends may underestimate them comparing to those
204 reported in the literature. Here, in order to investigate the potential differences on AOD and DOD temporal trends, a sensitivity
205 analysis using both geometric and arithmetic mean is established. MIDAS dataset includes negative DOD values introduced
206 from the applied Dark Target algorithm of MODIS AOD retrievals. Since zero or negative arguments of logarithm cannot be
207 defined, all these values are overwritten to 0.0001 as suggested by Sayer and Knobelspiesse (2019).

3 Results

209   This section is divided into three main parts. Sect. 3.1 describes the geographical distribution of AOD and DOD trends,
210 at global scale, by performing simultaneously a sensitivity analysis on: (i) the aggregation metric (geometric vs. arithmetic
211 mean), (ii) the spatial resolution (fine vs. coarse), (iii) MIDAS trends evaluation (DOD vs. cAOD trends), and (iv) the applied
212 temporal criteria (filters vs no filters). In Sect. 3.2, focus is given on the seasonal DOD trends whereas in Sect 3.3 emphasis is
213 given on DOD trends at 12 regions of interest.

3.1 Global trends

3.1.1 Geometric vs. arithmetic mean

216   The overwhelming majority of the published AOD/DOD trend analysis studies have been relied on arithmetic mean in
217 order to produce coarser spatial (e.g. 1° x 1°) and temporal (e.g. monthly values) resolutions. In this study, a sensitivity analysis
218 on the aggregation method (i.e. arithmetic vs geometric mean), has been performed by utilizing the daily coarse spatial
219 resolution (1° x 1°) MIDAS DODs. Figure 1 depicts the frequency histogram of MIDAS DODs in log scale using all the
220 available data over the period 2003–2017. It is apparent that the shape of the DOD distribution is close to a log-normal

221 distribution (Fig. 1). The latter considers the extreme dust episodes which force the distribution curve to be right-skewed.

222 Arithmetic mean is about 4 times higher than the geometric mean, highlighting the importance of which metric is more

223 representative of the population and how this can affect the results for specific applications (e.g. radiative forcing). When

224 geometric standard deviation is considered, 65.43% of DOD values range between 0.002 and 0.027 while 81.04% encompassed

225 within –0.033 and 0.099 for arithmetic mean, indicating an overstating of the variability (Sayer and Knobelspiesse, 2019). The

226 averages and the standard deviations are calculated using weighted aggregation exrpessions with the weighting factors in terms

227 of latitude (see Sect. 2.3). An additional point, revealing that the selection of normal statistics can lead to a misrepresentation

228 of the population for a positive-definite quantity (i.e. dust optical depth), is that the lower bound (−0.033) is negative, which

229 has not any physical meaning.

230
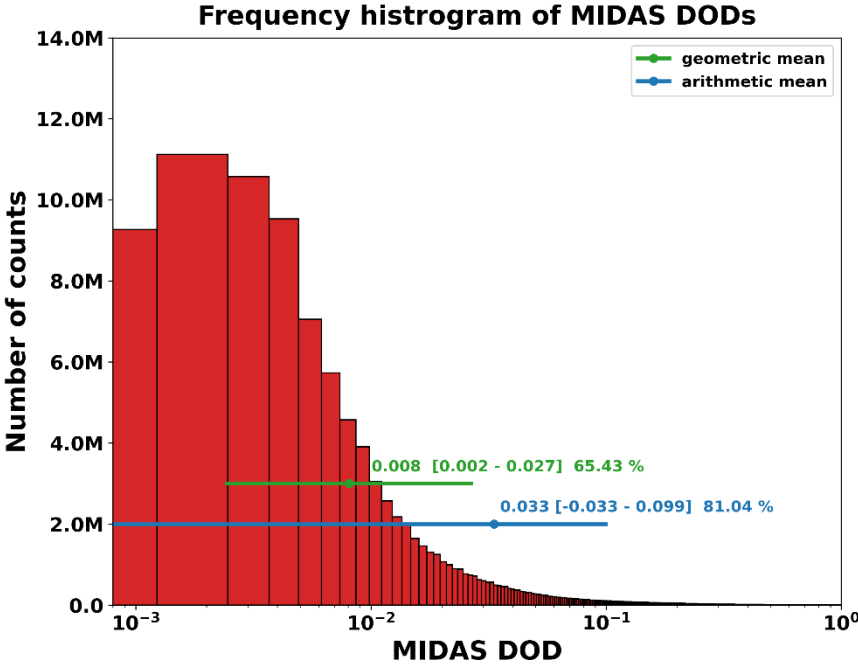
Figure 1. Frequency histogram of MIDAS DODs reported at 1° x 1° spatial resolution over the period 2003 – 2017. The computed geometric mean (green) and arithmetic mean (blue) are given along with ranges corresponding to geometric mean/geometric standard deviation and geometric mean*geometric standard deviation for the geometric mean and ± standard deviation for the arithmetic mean.

235 In agreement with Sayer and Knobelspiesse (2019), the calculated trends for AOD and DOD are consistent in terms of

236 sign between fine (Fig. 2) and coarse (Fig. 3) spatial resolution data. However, in terms of magnitude this is not the case.

237 Figure S1, S2 depicts the frequency histograms of the deviations between the arithmetic and geometric trends. When geometric

238 AOD/DOD averages are considered, the deseasonalized trends are suppressed by up to 91.77% with the respect to the

239 corresponding levels obtained from the arithmetic means, regardless the underlying surface type. The only exception is found

240 for AOD at 1° spatial resolution and across oceanic territories (Fig. S2c) where geometric trends overestimate those of

241 arithmetic by 71.63%.

242

243
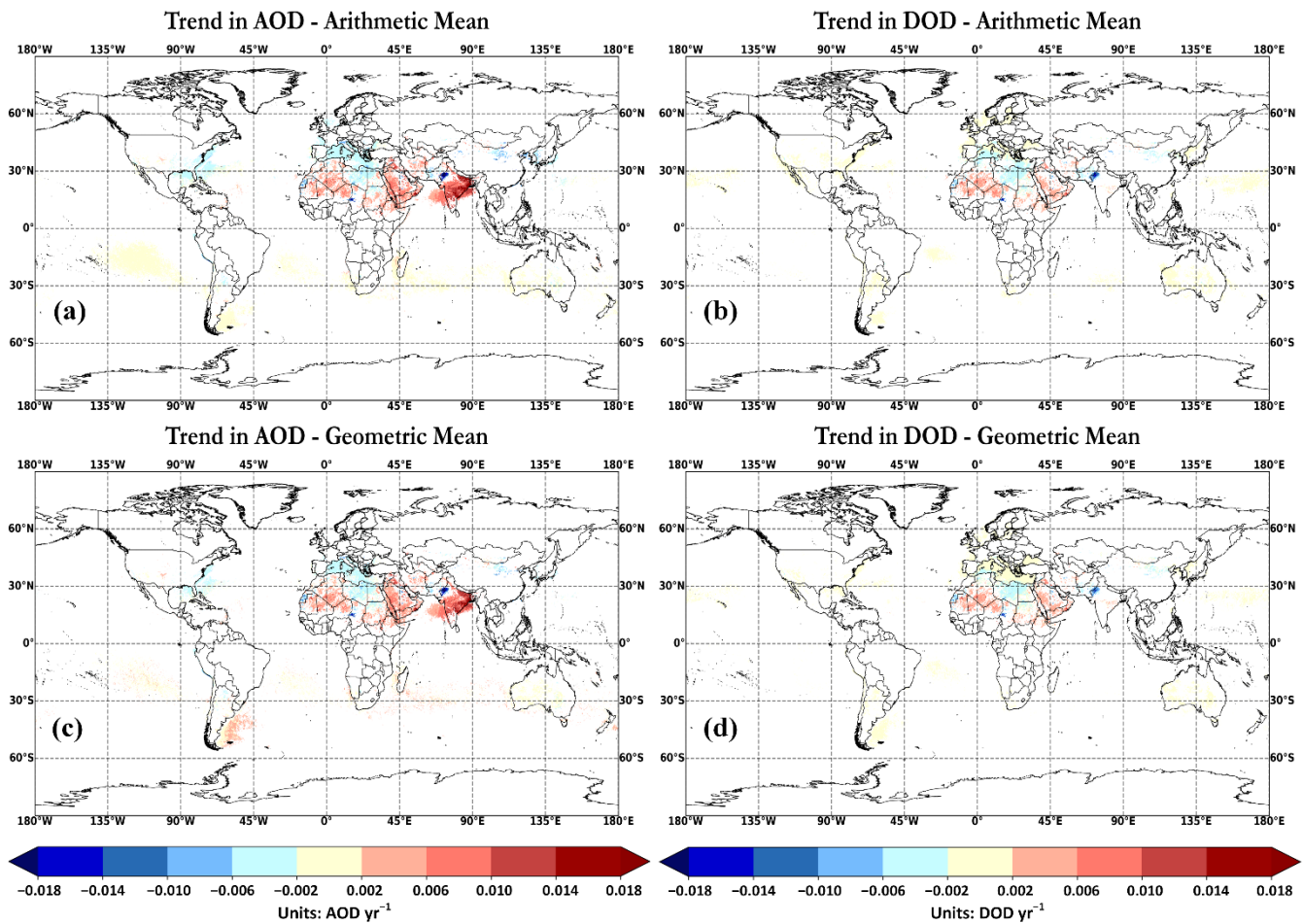
Figure 2: Global maps of temporal trends (statistically significant at 95% confidence level), at 0.1° x 0.1° spatial resolution, calculated from the deseasonalized AOD (a and c) and DOD (b and d) monthly values during 2003 – 2017. Upper panel (a, b) shows the arithmetic-based trends while the bottom panel (c, d) indicates the geometric-based trends. The pixels with: 1) non-significant trends, 2) the temporal criteria are not met and 3) not available data are colored as white (blank) in each map of trend analysis. Neutral trends, ranging between −0.002 and 0.002 DOD yr^{-1}, are colored with light yellow (or cream) (the central color of the color bar). Figs S3a, S3b and S4 present the differences between the aforementioned colors at fine, coarse spatial resolution as well as for the seasonal trends, respectively. Based on those Figs, the pixels with not available data are colored with gray color while those of failing to meet the availability criteria are colored with greenish.

252
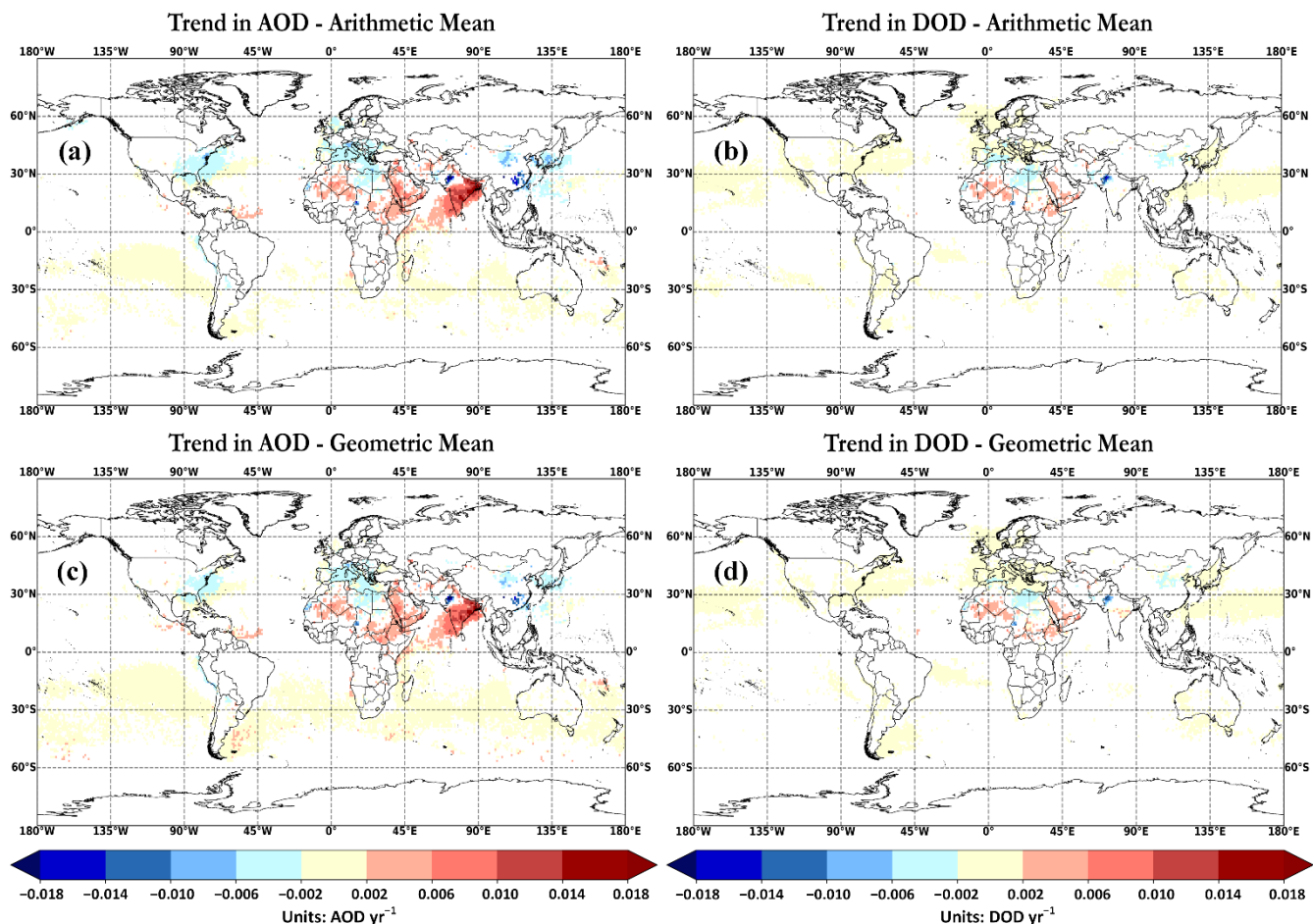
Figure 3: Same as Fig. 2 at 1° x 1° spatial resolution.

Across the dust-affected regions of the planet, the calculated AOD and DOD trends have revealed similar pattern. Over areas where the dust contribution to the total aerosol load is negligible, DOD trends are non-significant or neutral. For instance, strong positive AOD trends are depicted across India and the Bay of Bengal (Figs. 2a and 2c), whereas the recorded annual DOD tendencies are negligible (Figs. 2b and 2d). Similar findings are evident along the eastern coasts of US and in the Gulf of Mexico. In the Mediterranean Basin, engrossing disparities are recorded between AOD and DOD trends. Negative AOD trends are shown in the entire region with decreasing DOD trends confined in the southern areas near the North Africa coast (Figs. 2b and 2d). In addition, strong positive trends for AOD and DOD are revealed in Central Sahara (up to 0.026 yr^{-1}), across Mauritania-Algeria-Mali-Niger areas and the Arabian Peninsula. The highest positive tendencies are shown in Oman−Saudi Arabia borders (up to 0.031 yr^{-1}). On the contrary, decreasing AOD/DOD tendencies are observed in the Eastern (down to −0.017 yr^{-1}) and Western (down to −0.019 yr^{-1}) Sahara, in the Bodélé Depression of the Chad Basin (northern of Lake Chad), in the Gobi Desert (Northern China−Southern Mongolia) as well as in the Thar Desert (northwestern Indian subcontinent). Among the regions where declining tendencies are evident, the most negative ones are recorded in the Bodélé

267 Depression (down to -0.025 yr^{-1}) and in the Thar Desert (down to -0.029 yr^{-1}). A comprehensive regional analysis including

268 the intercomparison with prior findings and the potential trends justification is discussed in Sect. 3.3.

269

3.1.2 Fine vs. coarse spatial resolution

271 The second sensitivity analysis aims to highlight differences of AOD/DOD trends when fine and coarse spatial resolution

272 of MIDAS data are contrasted. De Meij et al. 2012 have investigated the differences between the fine daily MODIS AOD (L2;

273 at 0.1° x 0.1° spatial resolution) and the coarse monthly MODIS AOD (L3; at 1° x 1° spatial resolution) in trend calculations

274 utilizing the Collection 5 (C005) retrievals. According to their study, a good agreement was found between the L2 and L3

275 AOD trends over specific areas (i.e. Central Mediterranean, North-East America, and East Asia). At a first glance, the trend

276 patterns reproduced by the fine (Fig. 2) and coarse (Fig. 3) MIDAS DODs are spatially consistent. Nevertheless, in terms of

277 magnitude, the absolute values of DODs at coarser spatial resolution are lower in most of areas with evident signal (either

278 positive or negative), such as the southern parts of the Arabian Peninsula (up to 0.014 yr^{-1}), the Bodélé Depression (down to

279 -0.015 yr^{-1}) and the Thar Desert (down to -0.024 yr^{-1}). Coarser grid-cells in contrast to the finer spatial resolution meet the

280 data availability threshold ($\geq$ 60 months) (Fig. S3) defined for the calculation of temporal trends because of their more

281 extensive spatial coverage. MIDAS meets adequately the temporal criteria (Sect. 2.2) both at fine (Fig. S3a) and coarse (Fig.

282 S3b) spatial resolutions, providing grid cells of long-term AOD/DOD time series along with significant AOD (Figs. 2a, 2c, 3a

283 and 3c) and DOD (Figs. 2b, 2d, 3b and 3d) tendencies. Trend analysis for the coarse grids yields a superior number of

284 significant AOD tendencies globally (Figs. 3a and 3b). For instance, new and significant declining coarser AOD trends are

285 observed in East Asia, particularly across Southeast Asia, the Yellow Sea, the Sea of Japan, and the North Pacific Ocean.

286 Similarly, new increasing AOD trends are reported in the Southern Arabian Sea and the North Atlantic Ocean nearby the coast

287 of Venezuela.

288 Voss and Evan (2020) generated two global DOD datasets using MODIS retrievals, combined with reanalysis data and

289 AERONET inversion retrievals. They estimated the decadal DOD trends (see their Figs. 11a and 11b) based on MODIS/Terra

290 (2001−2018) and MODIS/Aqua (2003−2018) data projected at an equal lat-lon 1° spatial resolution. In order to compare the

291 findings in this study against Voss and Evan (2000), only arithmetic DOD trends are used at the same grid-cell spatial resolution

292 (Fig. 3b). In addition, since MIDAS dataset relies on MODIS-Aqua retrievals (Sect. 2.1), only their DOD MODIS/Aqua dataset

293 is used for comparison. Table 1 displays the ranges of DOD trends between the two datasets over 15 desert and downwind

294 areas of the globe. The selection of the above regions is accomplished based on the areas in which statistically significant DOD

295 trends are revealed in Voss and Evan (2020) study. Over the Sahara Desert, Bodélé Depression and Thar desert, identical

296 significant trends in terms of magnitude and sign are recorded in both studies. Over Arabian Peninsula, the calculated trends

297 here are common in terms of sign but lower in terms of magnitude. More specifically, the current study reports declining DOD

298 trends along the Mediterranean Basin, while Voss and Evan (2020) did not find any significant trends. On the other side, they

299 reported strong positive trends over Tropical Atlantic Ocean, sub-Sahel, Northeast Middle East and Northeast Caspian and

300 Aral Sea which is not the case here. Trend inconsistencies are revealed because of a) the derivation algorithm of DOD, b) the

301 trend detection methodology, c) the different study periods, and d) the temporal filtering criteria.

302 **Table 1: Comparison of the computed DOD trends between the current study and the Voss and Evan (2020) over 15 regions of**
303 **interest.**

Regions	Latitude (•)	Longitude (•)	Current study (DOD yr^{-1})	Voss and Evan (2020) (DOD yr^{-1})
Desert areas				
West Sahara	21 – 26 N	12 – 16 W	–0.010 - – 0.002	–0.010 - –0.002
Central Sahara	15 – 30 N	10 W – 15 E	0.002 - 0.010	0.002 - 0.010
East Sahara	18 – 30 N	15 – 30 E	–0.006 - – 0.002	–0.006 - – 0.002
Bodélé Depression	13 – 16 N	12 – 18 E	–0.018 - – 0.002	–0.018 - – 0.002
Middle East	10 – 35 N	35 – 50 E	0.002 - 0.018	0.002 - 0.021
Thar Desert	24 – 30 N	68 – 76 E	–0.018 - – 0.002	–0.021 - – 0.002
Gobi Desert	37 – 45 N	90 – 110 E	–0.006 - – 0.002	–0.010 - – 0.002
Downwind areas				
Sub-Sahel	0 – 13 N	60 W – 20 E	Non-significant	0.002-0.018
Mediterranean Basin	30 – 45 N	10 W – 30 E	–0.006 - – 0.002	–0.002 - 0.002
Region surround Caspian Sea	35 – 60 N	45 – 60 E	Non-significant	0.002 - 0.021
Tropical Atlantic Ocean	0 – 15 N	20 – 60 W	Non-significant	0.002 - 0.006
South Atlantic Ocean	30 S – 0	13 W – 13 E	Non-significant	–0.006 - 0.006
North Pacific Ocean	40 – 60 N	140 E – 120 W	Non-significant	–0.010 - – 0.010
North Pacific and North America	15 – 40 N	140 E – 75 W	–0.002 - 0.002	–0.002 - 0.002
South Pacific Ocean	45 – 15 N	160 E – 80 W	–0.002 - 0.002	–0.002 - 0.002

304

305 3.1.3 Evaluation of MIDAS trends vs. AERONET

306 The validity of the computed MIDAS DOD trends is thoroughly analyzed in this section. For evaluation purposes, the

307 coarse mode AOD, hereafter referred as cAOD, retrieved through the AERONET SDA algorithm is applied. The two datasets

308 are collocated by spatially averaging MIDAS DODs included in an area of 3x3 pixels around each AERONET site, and also

309 temporally combined using solely the same daily values. DOD and cAOD trends are calculated using the methodology

310 described in Sect. 2.3. Figure 4a illustrates the geographical distribution of the AERONET stations (in total 41) satisfying the

311 defined temporal criteria (see Sect. 2.3) and finally used in the assessment analysis. According to Fig. 4b, a good linear
312 correlation (R = 0.86) of the derived trends is observed accompanied with low bias (MBE = −0.04x10^{-2}). In order quantify the
313 performance of MIDAS in capturing the cAOD trends, the total accuracy (TA) of the correct trends (identical sign) is
314 calculated. More specifically, TA is defined as the percentage of the stations with correct trends sign (the sum of B1 and A2
315 quadrants numbers in Fig. 4c divided by the total number of stations). MIDAS trends can capture the correct cAOD trends
316 signs with a TA of 80.5% (Fig. 4c). In addition, the percentages of each quadrant in Fig. 4c shows the number of the correctly
317 detected stations per sign. The overwhelming majority of the AERONET stations encompassed negative trends (30 out of 41
318 stations). MIDAS trends capture the 26 out of those 30 (86.7%) stations denoted with negative cAOD trends. Lastly, there are
319 only 11 sites with positive cAOD trends, and MIDAS proved able to detect them at 7 out of 11 (63.6%) stations.

320
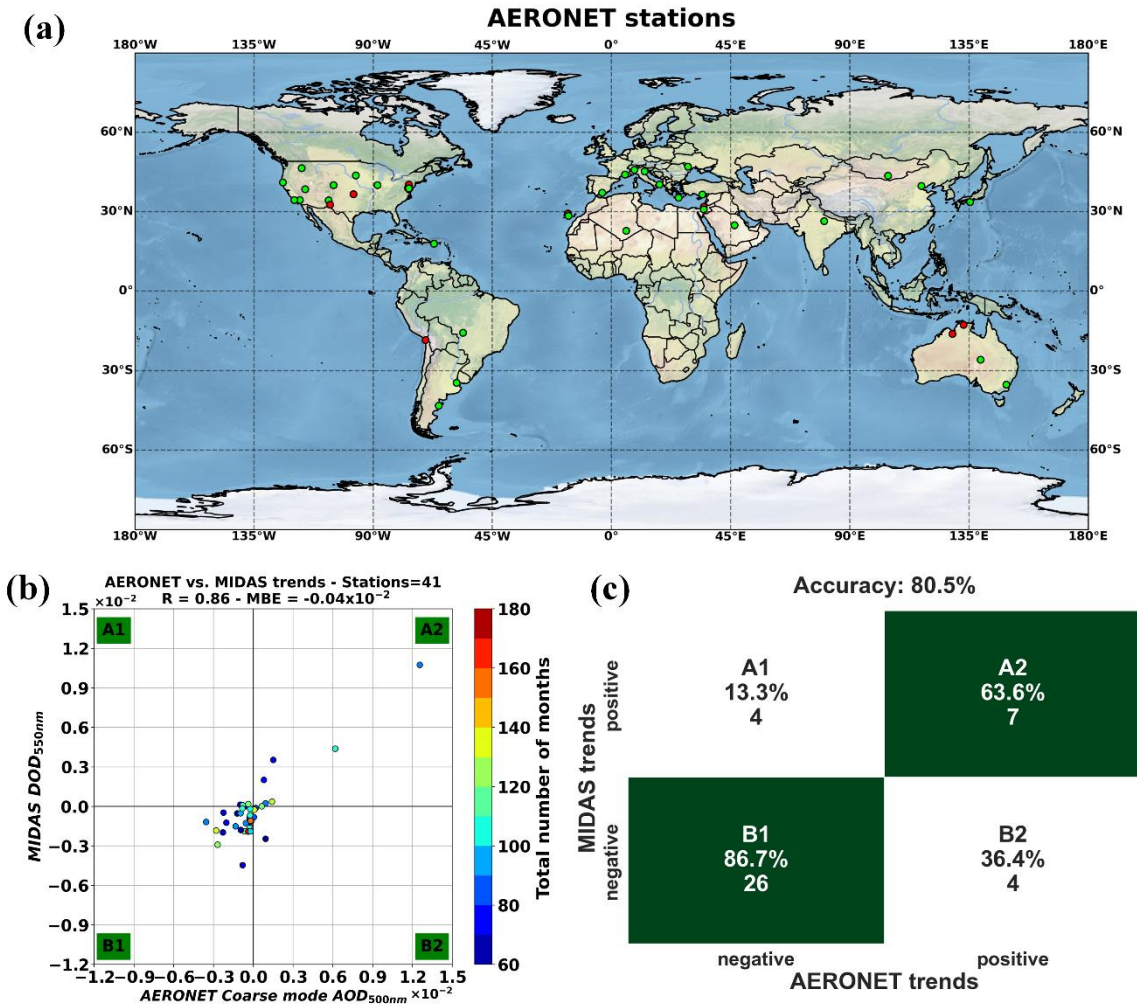
343 **Figure 4: (a) Geographical location of the available AERONET stations in which the temporal trends of DOD and cAOD are**
344 **calculated. Green and red dots refer the stations with the similar and different trend sign, respectively. (b) Scatter plot between**

MIDAS DOD and AERONET cAOD trends. The color bar indicates the total number of months. (c) Confusion matrix of possible trend signs among the two datasets.

Table S1 provides the point-to-point trend results for each collocated MIDAS-AERONET sites. It should be mentioned that among the revealed stations, few indicate dust particles as the predominant aerosol type. Based on Logothetis et al. (2020), the station of Solar Village, Arabian Peninsula, is primarily a "dusty" site revealing significantly high percentages of coarse absorbing particles. Across this station, the trends between AERONET cAOD (0.0126 yr^{-1}) and MIDAS DOD (0.0107 yr^{-1}) are in good agreement in terms of magnitude, but both are non-significant at the 95% confidence level. Similar findings are also observed in the "dusty" site of Tamanrasset, Algeria, showing increasing cAOD and DOD trends of 0.0062 yr^{-1} and 0.0044 yr^{-1}, respectively. One of the advantages of MIDAS is that it provides the dust aerosols burden information in downwind regions of the planet. For instance, most of the stations located in South Europe receive dust particles transported towards the Mediterranean from Sahara and Middle East deserts, encompassing identical trend signs (Fig. 4a). Moreover, there are many downwind regions across different regions of the globe with similar trends magnitude such as Ispra, Italy (cAOD= -0.0013 yr^{-1}, DOD= -0.0015 yr^{-1}), Kanpur, India (cAOD= -0.0027 yr^{-1}, DOD= -0.0029 yr^{-1}), SERC (cAOD= -0.0023 yr^{-1}, DOD= -0.0020 yr^{-1}) in US, Shirahama, Japan (cAOD= -0.0020 yr^{-1}, DOD= -0.0012 yr^{-1}), and XiangHe, China (cAOD= -0.0028 yr^{-1}, DOD= -0.0018 yr^{-1}).

3.1.4 Filtering vs. non-filtering trends

The third sensitivity analysis of this section concerns the calculation of temporal trends using filtered (Fig. 2) and non-filtered (Fig. 5) data at fine spatial resolution. Here, the AOD/DOD trends are calculated by applying two consecutive temporal filters (Sect. 2.3). More specifically, the two applied temporal filters include the: 1) the calculation of the monthly averages when at least 6 days are available and 2) the trend calculation only in grid cells with higher than 60 available months (5 years). The total number of grid points for trend calculation increases when the above two temporal filters are not applied. Overall, months with more than one daily measurement are retained for trend analysis, increasing the total data availability of the entire global grid from 36% (filtered) to 83% (non-filtered).

370
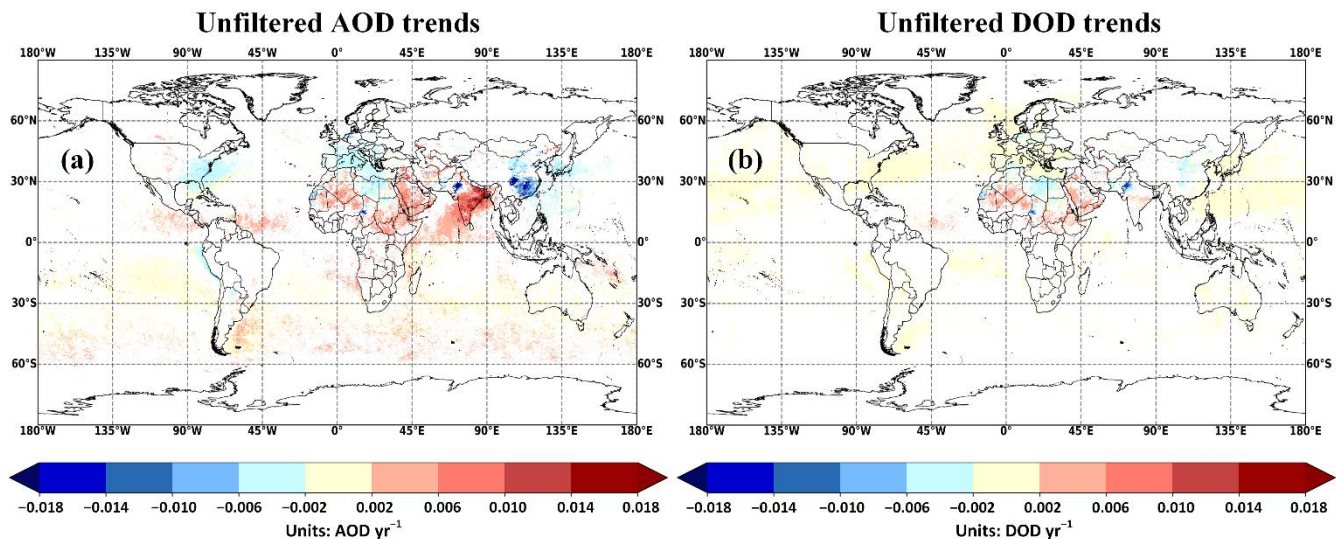
Figure 5: Global maps of unfiltered temporal trends (statistically significant at 95% confidence level), at 0.1° x 0.1° spatial resolution,
calculated from the deseasonalized geometric (a) AOD and (b) DOD monthly values during 2003 – 2017.

According to Eq. (3), σ_ω (Fig. S5) and the statistical significance (Fig. S6) of the trend are controlled by σ_N, φ (Fig. S7) and n (Fig S3). The differences in data availability between the unfiltered and filtered trend analysis are depicted in Fig. S8. Across the desert areas, the number of filtered months is adequately high and very close to the non-filtered case (Fig. S8). Thus, no trend differences in magnitude and sign are recorded. Over maritime and continental dust affected areas, new statistically significant AOD and DOD trends are represented when the unfiltered data are employed. Firstly, the number of pixels with statistically significant DOD trends has been significantly increased (Fig. 5b) but the majority of the new trends are mainly neutral located over oceanic territories (yellow pixels). New positive DOD tendencies are observed over Tropical Atlantic and India while new negative trends are recorded across Southeast China (Fig. 5b). Secondly, the significant AOD trends grid points are also strongly increased. New decreasing AOD trends are observed over USA, China and Philippine Sea (Fig. 5a). Especially across the region of southeastern China, the number of significant AOD trends has been increased profoundly. In addition, new AOD increasing trends are recorded over Tropical Atlantic, North Pacific (West of Mexico), Arabian Sea and the oceanic area between 30.0ºS and 60.0ºS. Despite the increase in monthly data availability, trend analysis without temporal filtering may lead to erroneous and not representative results either for AOD or DOD. In order to investigate in detail the last statement, a sensitivity analysis is performed using in total 76 AERONET stations (Fig. S9a). Through the evaluation analysis of MIDAS DOD trends (Sect. 3.1.3), the AERONET stations have been selected based on their data availability. More specifically, only the stations with at least 10 years of data have been retained for further analysis. Tahe total number of sites has been decreased from 76 (here) to 41 due to temporal filtering (see Sect. 3.1.3). Based on Fig. S9b, the unfiltered temporal trends between MIDAS and AERONET documented a profoundly lower linear correlation (R=0.51) while

391 the data points are more sparse. When trends are calculated without any temporal filtering, the total accuracy of the correct

392 trends has been decreased from 80.5% (Fig. 4c) to 73.7% (Fig. S9c).

393 In the following sections, and considering all three implemented sensitivity analysis, only the geometric-based DOD and

394 AOD trends (Sect. 3.1.1) at fine spatial resolution (Sect. 3.1.2) including the temporal filtering (Sect. 3.1.4) are discussed.

395

3.2 Seasonal trends

397 Dust aerosols' burden is subjected to strong intra-annual and interannual variations with different cycles depending on the

398 source or downwind region (Gkikas et al., 2021b). Here, the seasonal DOD tendencies at a global scale (Fig. 6) are calculated

399 based on the methodology proposed by Hsu et al. (2012). The corresponding seasonal AOD trends are depicted in Fig. S10.

400
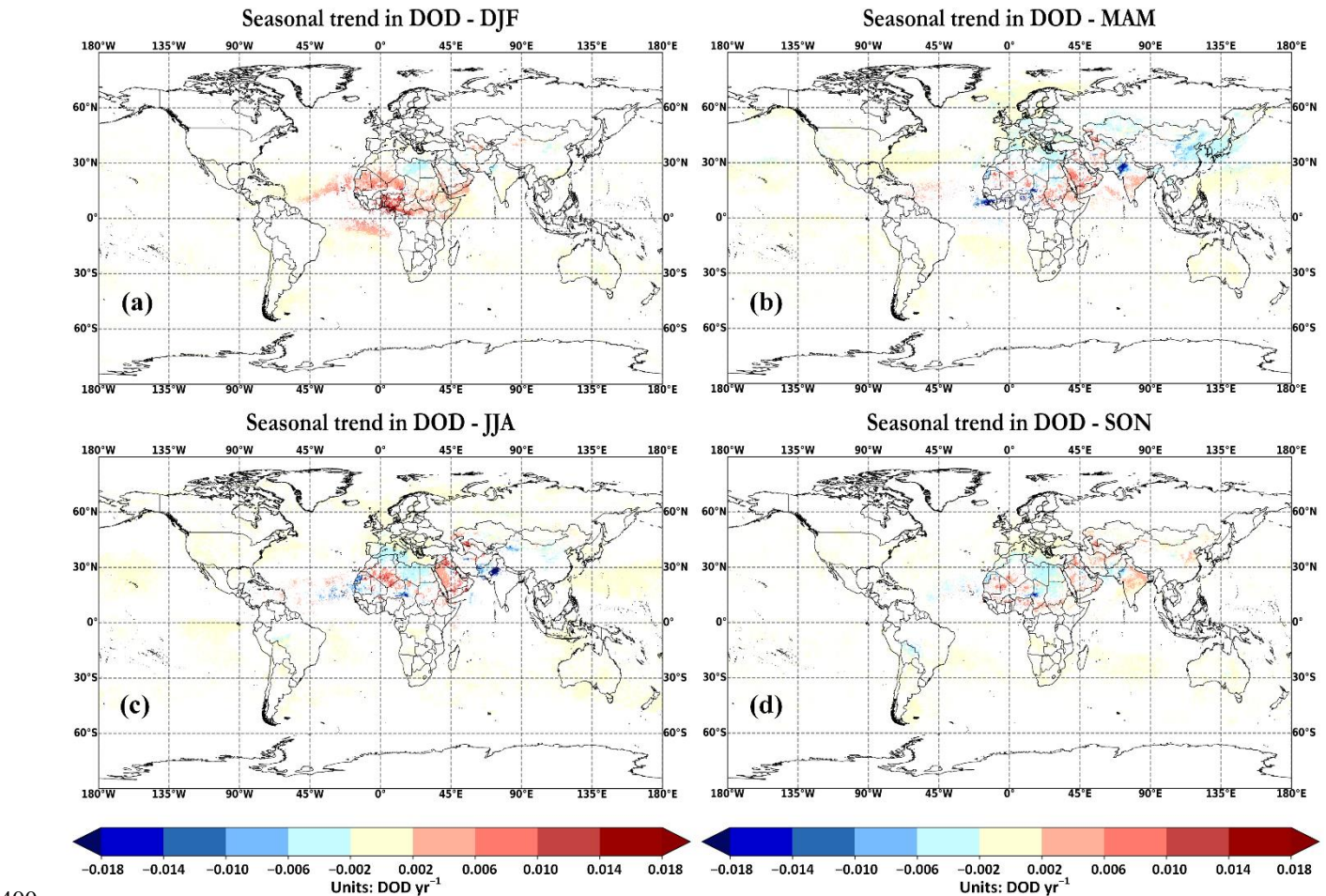
401 **Figure 6: Seasonal geographical distributions of DOD temporal trends at (a) December-January-February (DJF), (b) March-April-**
402 **May (MAM), (c) June-July-August (JJA) and (d) September-October-November (SON).**

403   The detection of the statistical significance of the calculated trends based on Weatherhead et al. (1998) cannot be applied
404 here due to the 9-month gap among the seasons. Therefore, an alternative approach is followed by calculating the seasonal
405 trends using a simple linear regression model on the DOD anomalies and identifying the statistically significant trends based
406 on the two-sided Student's t-test. The null hypothesis of the t-test assumes a non-significant temporal trend under a defined
407 confidence level (here is 95%). The total number of months for each season is displayed in Fig. S4. Only the grid points with
408 more than 13 available months (13 from 45 total months) are retained. The performed analysis at global scale and on a seasonal
409 basis highlights many regions with significant DOD trends (Figs. 2 and 6) which are used to define regional domains (Fig. 7).
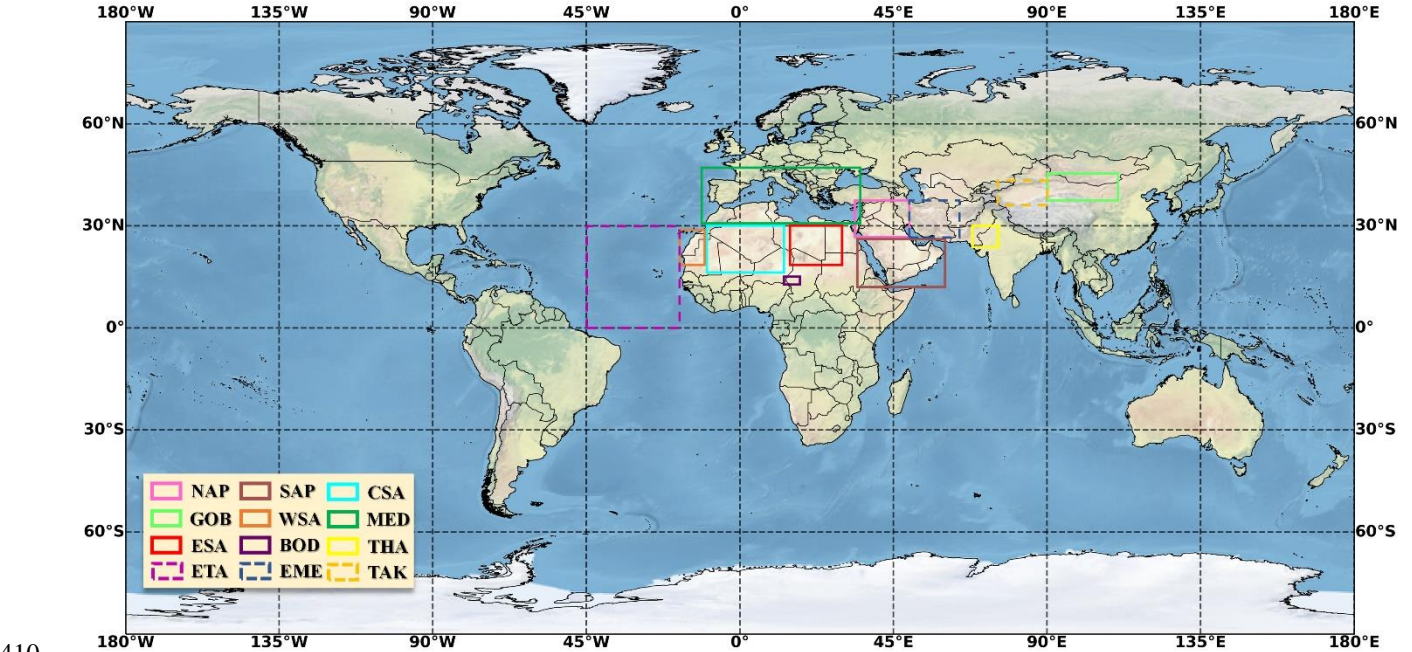
410

411 **Figure 7: Regions of interest for seasonal and regional analysis: North Arabian Peninsula (NAP), South Arabian Peninsula (SAP),**
412 **Central Sahara (CSA), Gobi Desert (GOB), West Sahara (WSA), Mediterranean (MED), East Sahara (ESA), Bodélé Depression**
413 **(BOD), Thar Desert (THA), East Tropical Atlantic (ETA), Eastern Middle East (EME) and Taklamakan Desert (TAK). Solid**
414 **rectangles indicate the regions which are included in the regional analysis (Sect. 3.3) while solid and dashed rectangles are for the**
415 **seasonal analysis.**

416   The Sahara Desert, hosting some of the most active aeolian natural dust sources of the planet, is a region of great interest
417 for investigating the intra-seasonal DOD variations. In its central sector, increasing trends are recorded throughout the year
418 (maximum positive value in JJA) (Table 2). On the contrary, negative seasonal DOD trends appear in the majority regions
419 across North Africa (Fig. 6). The western and eastern parts of the Sahara Desert present strong declining trends maximized
420 during boreal summer (Table 2). From spring to autumn, in the Bodélé Depression, substantial decreasing trends are recorded
421 (Table 2). Over the period 2001−2012, dust emissions in the broader area of the Bodélé Depression were decreased in
422 summertime, which was attributed to the increased rainfall, caused by the positive trends of the Sahara heat lows (SHL), the
423 warm phase of Atlantic Multi-decadal Oscillation (AMO) and the decreasing trends in terms of occurrence and intensity of

nocturnal low-level jets' (NLLJ) (Shi et al., 2021). Surface wind speed also affects dust emissions across North Africa (Evan et al., 2016). Surface wind speed and NLLJ are the principal drivers for the interannual variation of dust emissions across Western Sahara, while in summertime dust emissions decreased during 2001−2012 (Shi et al., 2021). The eastern sector of North Africa (North Libya and Egypt) presents moderate negative trends maximized in winter (down to −0.014 yr^{-1}) and spring (down to −0.011 yr^{-1}). In the western sector (i.e. north Algeria and Tunisia) strong significant declining trends are observed in summer (down to −0.035 yr^{-1}) (Fig. 6c). The dust sources residing near the North African coasts are strongly influenced by the surface wind speed, NLLJ, Harmattan surge and the tracks of the Mediterranean depressions (Shi et al., 2021).

Table 2: Seasonal trends over 12 regions of interest. Each column includes: the range of DOD trend (yr^{-1}) and the median DOD trend. Non-available values are shown in blank cells. The domains of the regions are depicted in Fig. 7.

Region	Winter (DJF)	Spring (MAM)	Summer (JJA)	Autumn (SON)
Central Sahara Desert	−0.007-0.017, 0.004	−0.025-0.027, 0.007	−0.018-0.031, 0.007	−0.014-0.019, 0.005
Western Sahara Desert	−0.009-0.013, 0.004	−0.021-0.022, −0.006	−0.028-0.017, −0.008	−0.016-0.009, −0.004
Eastern Sahara Desert	−0.011-0.007, −0.003	−0.017-0.013, −0.004	−0.020-0.012, −0.003	−0.014-0.006, −0.003
Bodélé Depression		−0.038-0.015, −0.014	−0.025-0.014, −0.011	−0.028-0.011, −0.011
North Arabian Peninsula	−0.011-0.005, −0.003	−0.016-0.026, −0.003	−0.019-0.026, 0.005	−0.010-0.016, 0.004
South Arabian Peninsula	−0.013-0.012, 0.002	−0.019-0.026, 0.006	−0.020-0.024, 0.006	−0.016-0.013, 0.003
East Middle East	−0.011-0.007, 0.002,	−0.022-0.020, 0.004	−0.032-0.016, −0.005	−0.025-0.013, 0.002
East Tropical Atlantic	−0.010-0.022, 0.003	−0.022-0.022, −0.002	−0.029-0.019, 0.00	−0.012-0.014, −0.002
Mediterranean	−0.014-0.009, −0.001	−0.032-0.009, −0.002	−0.035-0.011, −0.002	−0.015-0.004, −0.002
Thar Desert	−0.007-0.002, −0.004	−0.024-0.004, −0.012	−0.047-−0.001, −0.021	−0.013-0.003, −0.005
Taklamakan Desert	−0.005-0.010, −0.003		−0.027-0.019, −0.006	
Gobi Desert	−0.010-0.006, −0.002	−0.023-0.014, −0.005	−0.011-0.005, −0.002	−0.005-0.012, 0.001

Numerous studies have notified the Saharan transatlantic transport (Peyridieu et al., 2013; Alizadeh-Choobari et al., 2014c; Prospero et al., 2014; Gläser et al., 2015; Fréville et al., 2020; Gkikas et al., 2021b). Across the Gulf of Guinea and mid-Atlantic, relatively high DODs are documented in boreal winter, ranging from 0.1 to 0.2 (up to 0.6) (Gkikas et al., 2021b). According to Fig. 6a, strong positive DOD trends are shown over Gulf of Guinea (up to 0.047 yr^{-1}). In this season, strong northeasterly winds (Harmattan) transport intense loads of Saharan dust towards Nigeria and the Gulf of Guinea (Washington et al., 2006). However, the trend magnitude along the Gulf of Guinea as well as in the northern regions (from Ghana to Cameroon) seems to be unreliable due to the reduced performance of MDF, surface contamination in the received radiances by MODIS and to the co-existence of aerosols and clouds (Gkikas et al., 2021b). In order to investigate the reliability of MIDAS DOD in the above region, the seasonal trend analysis is implemented at the AERONET station of llorin, Nigeria. It worths mentioning that this station has not been included in evaluation analysis of Sect. 3.1.3, due to the low number of months (N=48<60). However, 32 out of 48 months lie in boreal winter, enabling the application of the methodology during this season. Both datasets represented increasing and statistically significant cAOD (0.011 yr^{-1}, |ω/σ$_{ω}$|=2.43) and DOD trends (0.021 yr^{-1},

446   $|\omega/\sigma_\omega|=3.74$). As expected, MIDAS revealed higher in magnitude trends than cAOD (approximately 2 times higher). In the

447   case of AOD (Fig. S10a), identical positive trends as DOD are shown in winter. Interestingly, substantial negative DOD trends

448   (down to -0.045 yr^{-1}) are recorded during springtime in an area among Guinea, Sierra Leone and North Atlantic Ocean (Fig.

449   6b), while positive tendencies are documented over Tropical Atlantic Ocean in DJF (Table 2). Over the region extended from

450   the North Atlantic Ocean to the Eastern Caribbean Sea (Lat: 10.0 °N−18.0 °N; Lon: 70.0 °W−45.0 °W), moderate positive trends

451   are documented predominantly in MAM (up to 0.010 yr^{-1}) and JJA (up to 0.008 yr^{-1}). Dust transport from North Africa along

452   the Atlantic Ocean reaches the Caribbean Sea, while summer DODs are intertwined with tropical Atlantic cyclone activity.

453   More specifically, Caribbean DOD during summer is negatively correlated to Atlantic accumulated cyclone energy and

454   Atlantic Meridional Mode index (Xian et al., 2020). In addition, dust aerosol burden originated form Sahara Desert is directly

455   related to tropical cyclones (TCS) over Tropical Atlantic Ocean, but their relationship is not unambiguously clarified (Evan et

456   al., 2006). Based on model simulations, Pan et al. (2018) investigated the role of dust aerosols for the genesis of TCs over

457   tropical Atlantic basin, by comparison of dust and non-dust model simulations. They revealed that dust amount is directly

458   related to TCs, revealing a bimodal pattern. More specifically, favorable conditions for TCs formation are documented by

459   increasing the midlevel moisture and decreasing the vertical wind shear while unfavorable conditions are encompassed by

460   decreasing the low-level vorticity and potential intensity.

461   Increasing tendencies, throughout the year, appear in the Middle East (Table 2), with few exceptions, particularly in the

462   northern Arabian Peninsula (Fig. 6). More specifically, the southwestern sector of Oman presents the highest increasing trends

463   for all seasons (up to 0.026 yr^{-1}). Similarly, high positive trends in MAM (up to 0.015 yr^{-1}) and JJA (up to 0.018 yr^{-1}) are

464   documented over the western part of Saudi Arabia. Negative tendencies are observed for all seasons at the north of the Oroug

465   Bani M'aradh Wildfire Sanctuary (South Saudi Arabia) including strongly negative DOD trends in summer (down to -0.020

466   yr^{-1}) and spring (down to -0.019 yr^{-1}). In the northern part of the Arabian Peninsula, positive trends are detected predominantly

467   in JJA and SON. Dust activity across the Arabian Peninsula is strongly influenced by the intensity of the northwesterly Shamal

468   winds, favored by the low precipitation amounts during summer (Yu et al., 2015). The temporally extended drought (Notaro

469   et al., 2015) along with the cooling of the Tropical Indian Ocean and the Mediterranean Sea temperatures (Yu et al., 2015),

470   leading to an enhancement of the Shamal winds, could regulate the summer DOD trends across Arabian Peninsula. During

471   springtime, La Niña events constitute the principal drivers for the dust activity by reducing the rainfall amounts over Rub' al

472   Khali Desert; one of the most active dust sources across the Arabian Peninsula (Yu et al., 2015). Strong positive trends (up to

473   0.026 yr^{-1}) are encountered in MAM and JJA over Iraq, while significant increasing trends are recorded for all seasons across

474   the eastern Iran, with the most evident ones in spring (up to 0.020 yr^{-1}). However, a hotspot of strong declining trends exists

475   in southeastern area of Iran (34.5°N, 54.5°E) with the most negative values in JJA (down to -0.029 yr^{-1}) and SON (down to

476   -0.025 yr^{-1}). Moderate negative DOD trends are documented during the summertime (down to -0.01 yr^{-1}) across the Alboran

477   Sea (western Mediterranean). The dust aerosol burden has also been decreased in the eastern part of Mediterranean Sea during

478   spring (down to -0.006 yr^{-1}, from Lybia and Egyptian coasts to Aegean Sea) and autumn (down to -0.005 yr^{-1}, across the

479   Gulf of Sidra).

480 Statistically significant positive DOD trends are detected across the intersection of Kazakhstan, Uzbekistan and
481 Turkmenistan, in the northeastern Caspian Sea shore. At all seasons, the DOD trends exceed 0.011 yr^{-1} while the maximum
482 trends are recorded in summer (up to 0.035 yr^{-1}) and spring (up to 0.019 yr^{-1}). These findings substantiate the positive decadal
483 DOD trends (~0.18 $decade^{-1}$) of Voss and Evan (2020) and could be attributed to the amount of drawdown (~−6.72 cm yr^{-1})
484 in the Caspian Sea level during 1996−2015 (Chen et al., 2017). Central, South and East Asia constitute another regions of
485 interest in which robust DOD trends are encountered (Fig. 6). The maximum negative values are depicted over the Thar Desert
486 in JJA and MAM (Table 2). It must be highlighted that the maximum decreasing trends are detected during the high-dust
487 season in the Thar Desert (Proestakis et al., 2018). The reduction of dust load during the pre-monsoon (MAM) could be
488 attributed to the increase of the rainfall and soil moisture levels, acting in favor of wet dust deposition as well as decreasing
489 the dust erosion (Pandey et al., 2017; Jin and Wang, 2018; Lakshmi et al., 2019). Moreover, reductions in dust emissions are
490 recorded during summertime, which are strongly linked to soil moisture and wind speed (Shi et al., 2021). In Northwest China
491 (Central Asia) lies the Taklamakan Desert, where non-significant annual trends are documented (Fig. 2). However, significant
492 seasonally negative DOD trends are observed (Fig. 6) particularly in summertime (Table 2). Additionally, over the Gobi Desert
493 and East Asia strongly negative DOD tendencies are documented mainly in spring (Fig. 6b), when the dust activity peaks
494 (Proestakis et al., 2018). The negative DOD trends across the Gobi Desert could be attributed to reduced dust emissions, caused
495 by the decrease of surface wind speed which has been recorded between 2010−2016 (Guo et al., 2019).

496 **3.3 Regional trends**

497 The regional DOD and AOD trends are calculated for 9 specific regions of interest (Table 3 and Fig. 7 solid rectangles)
498 as well as for the whole globe (GLB) and separately over land (GLB-L) and ocean (GLB-O) (Sect. 3.3.1). The full names of
499 each region as well as the calculated regional DOD trends and their uncertainties are included in Table 3. The comparisons
500 among the geometric vs. arithmetic aggregation method and coarse vs. fine spatial resolution are also investigated for the
501 regional DOD (Fig. 8a) and AOD (Fig. 8b) trends. On a regional basis, the temporal trends between the two spatial resolutions
502 are in very good agreement, corroborating de Meij et al. (2012). Since the statistical significance of the trends is strongly
503 influenced by the number of years and the study period, the regional DOD trends are also computed for different time periods
504 considering the systematic change of time period (number of years) and initial year (Fig. 9).

505
506
507
508
509
510
511
512

Table 3: Global and regional temporal DOD trends based on MIDAS dataset. The trends with the ratio $|\omega/\sigma_\omega|$ higher than 2.0 are statistically significance at 95% confidence level. The star symbol corresponds to statistically significant regions under the 95% confidence level. The domains of the regions are represented in Fig 7.

Region	Acronym	Trend (ω, DOD yr^{-1}) × 10^{-3}	Uncertainty (σ_ω) × 10^{-3}	$|\omega/\sigma_\omega|$
lobal land & ocean	GLB	0.022	0.12	0.19
Global land	GLB-L	0.082	0.25	0.33
Global ocean	GLB-O	−0.017	0.069	0.24
North Arabian Peninsula	NAP	0.60	1.3	0.45
South Arabian Peninsula	SAP	1.80	1.2	1.55
Central Sahara	CSA	2.1	0.87	2.4*
Gobi Desert	GOB	−0.71	0.39	1.8
West Sahara	WSA	−0.95	0.85	1.1
Mediterranean	MED	−1.1	0.30	3.8*
East Sahara	ESA	−1.8	0.61	3.0*
Bodélé Depression	BOD	−5.5	2.6	2.1*
Thar Desert	THA	−5.3	1.9	2.8*
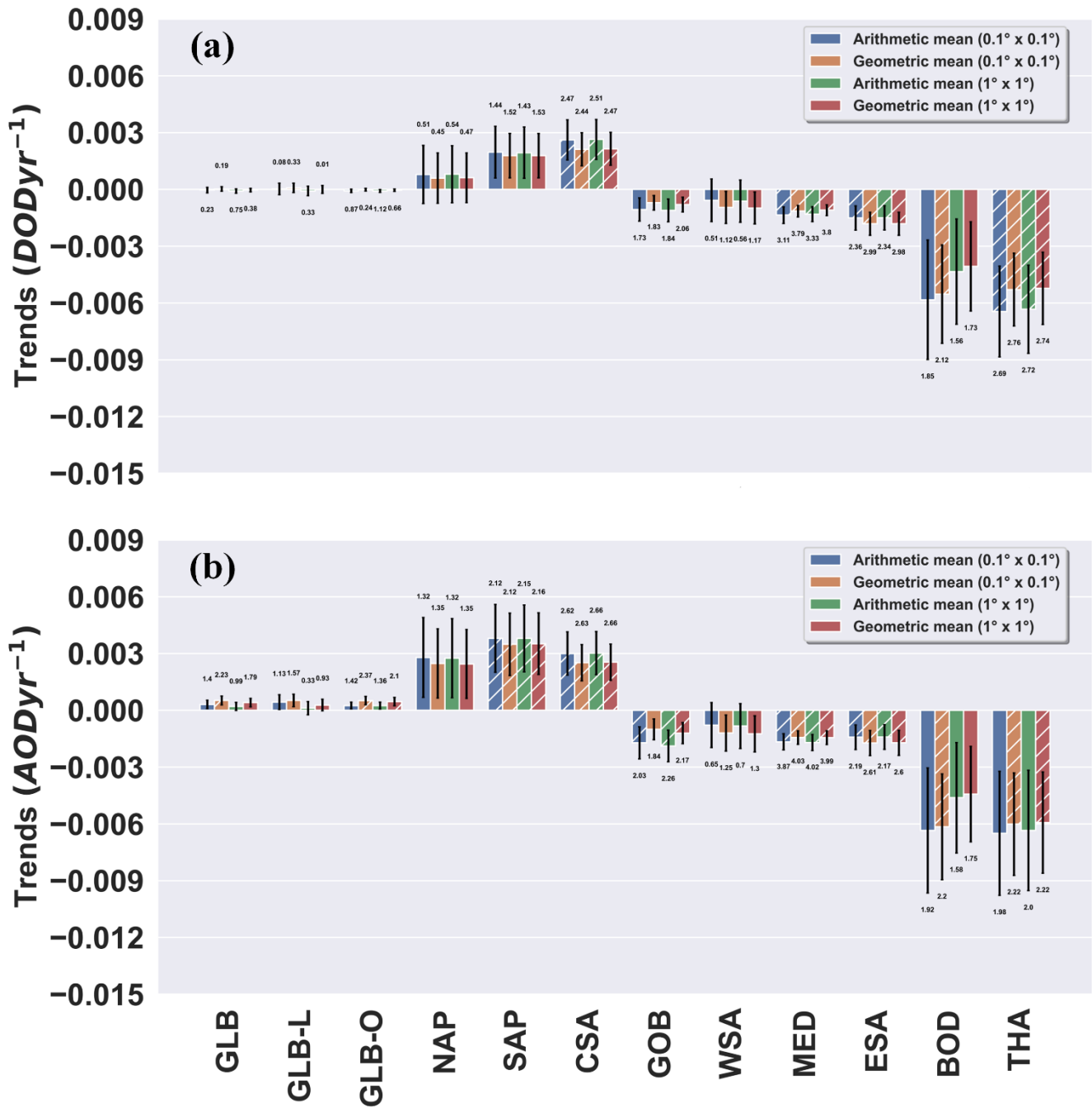
Figure 8: Bar-plots indicating the (a) DOD and (b) AOD regional temporal trends. The hatched bars represent regions with the significant trends ($|\omega/\sigma_\omega| > 2.0$). The error bars denote the uncertainty of the trends based on Eq. (3) (Sect. 2.3).

526 The explanation of the temporal evolution of calculated trends shown in Fig. 9 is presented in the next section for individual
527 regions.

528
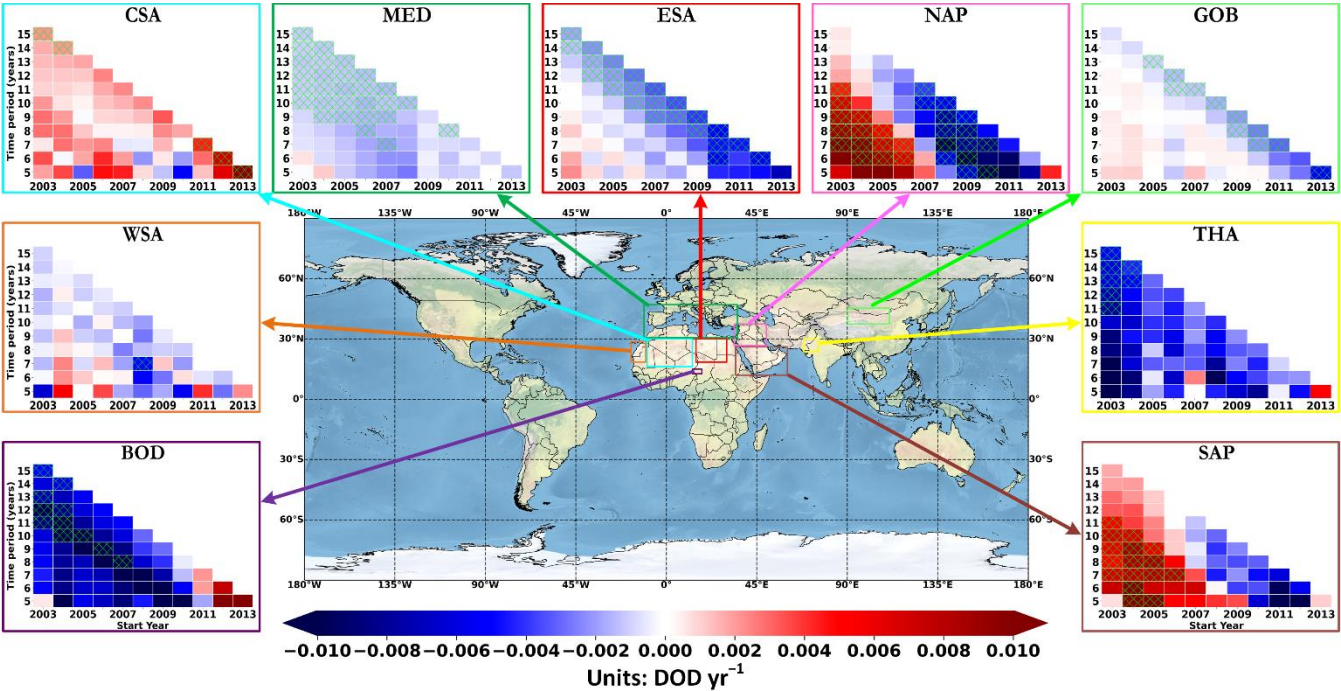
Figure 9: Regional DOD trends at different time intervals, with at least 5-year time series. The acronyms full names are documented in Table 3. YY' axis shows the number of trends included in the analysis, while XX' the starting year. The hatched pixels represent regions with the significant trends ($|\omega/\sigma_\omega| > 2.0$).

3.3.1 Global land and ocean

533   Small global DOD trends are recorded during the study period both over land and ocean (Table 3). However,
534 distinguishable DOD trends are detected at specific regions. Prior studies have focused on satellite-based measurements
535 detecting statistically significant AOD trends at global scale. Over oceanic areas, AOD trends based on MODIS Collection 6.0
536 are reported to be equal to 0.0050 decade^{-1} and 0.0020 decade^{-1} during 2000−2009 and 2000−2015, respectively (Alfaro-
537 Contreras et al., 2017). SeaWiFS AOD retrievals recorded higher annual positive significant trends over ocean (0.00080 yr^{-1})
538 for a 13-year period (1998−2010) (Hsu et al., 2012). Recently, significant positive tendencies are documented for GLB
539 (0.00066 yr^{-1}) using L3 Collection 6.1 MODIS/Terra measurements spanning from 2001 and 2016 (Che et al., 2019). In this
540 study, significant AOD trends of 0.00052 yr^{-1} and 0.00051 yr^{-1} are revealed over GLB-O and GLB respectively (Fig. 8b),
541 using geometric means at fine spatial resolution. The differences in trends magnitude among the studies are attributed to the
542 different datasets, aggregation methods and temporal availability.

3.3.2 North Africa

Across North Africa, four sectors have been defined based on the sign of the DOD trends (see Figure 7) The first one consists of Central Sahara (CSA) where increasing DOD trends are mainly recorded (up to 0.023 yr^{-1}) (Fig. 10c). Voss and Evan (2020) also reported similar DOD trends, in terms of sign and magnitude, based on MODIS/Aqua dataset over the period 2003−2018. At regional scale, positive significant DOD trends of 0.0021 yr^{-1} determining those of AOD as expected (regional DOD to AOD trend ratio=0.84) due to the predominance of mineral particles in the area among other aerosol species (Fig. 10d). During different time frames, the sign of DOD trends remains mainly positive (Fig. 9), with intense (from 0.0044 to 0.0095 yr^{-1}) and significant results within the 2011− onward periods. Nevertheless, the time window is very short to infer the amplitude of the calculated trends.

552
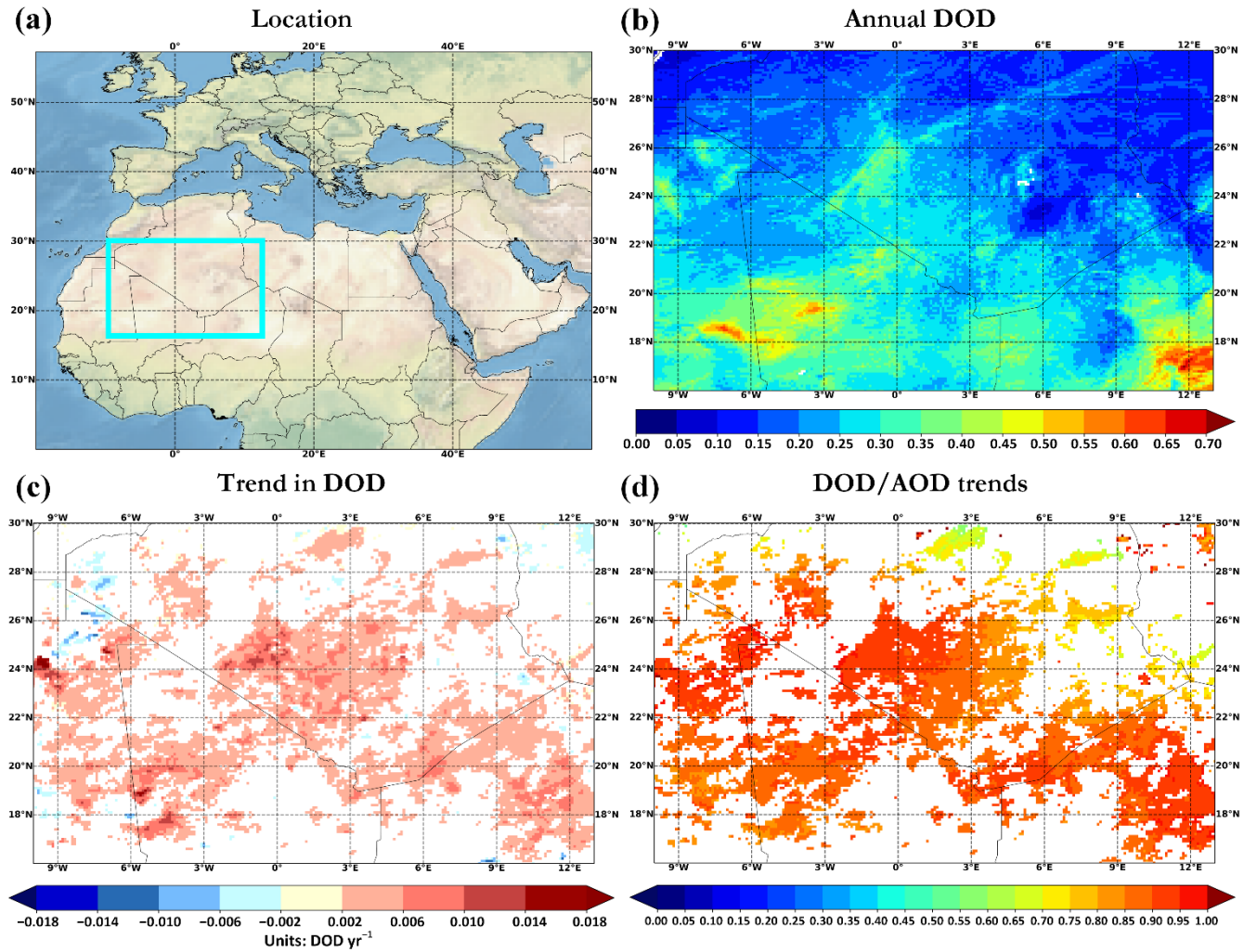
Figure 10: (a) geographical boundaries, (b) annual DOD, (c) DOD geometric trends and (d) DOD to AOD trends ratio, for the Central Sahara.

In the westernmost section of the Sahara Desert (WSA), in the majority of grid-cells (~73%) decreasing DOD tendencies are recorded (down to −0.015 yr⁻¹) whereas positive trends (up to 0.009 yr⁻¹) are evident at scattered pixels (~27%) within the domain (Fig. 11c). Overall, the total load (Fig. 8a) as well as the dust burden (Fig. 8b) have been decreased during the study period, but the magnitude of this reduction is relatively low and not statistically significant. This behavior is consistent regardless the spatial resolution or the approach for the calculation of regional values (i.e. arithmetic or geometric mean) (Figs. 8a and 8b). The same DOD trend pattern is also reflected using different time periods (Fig. 9).
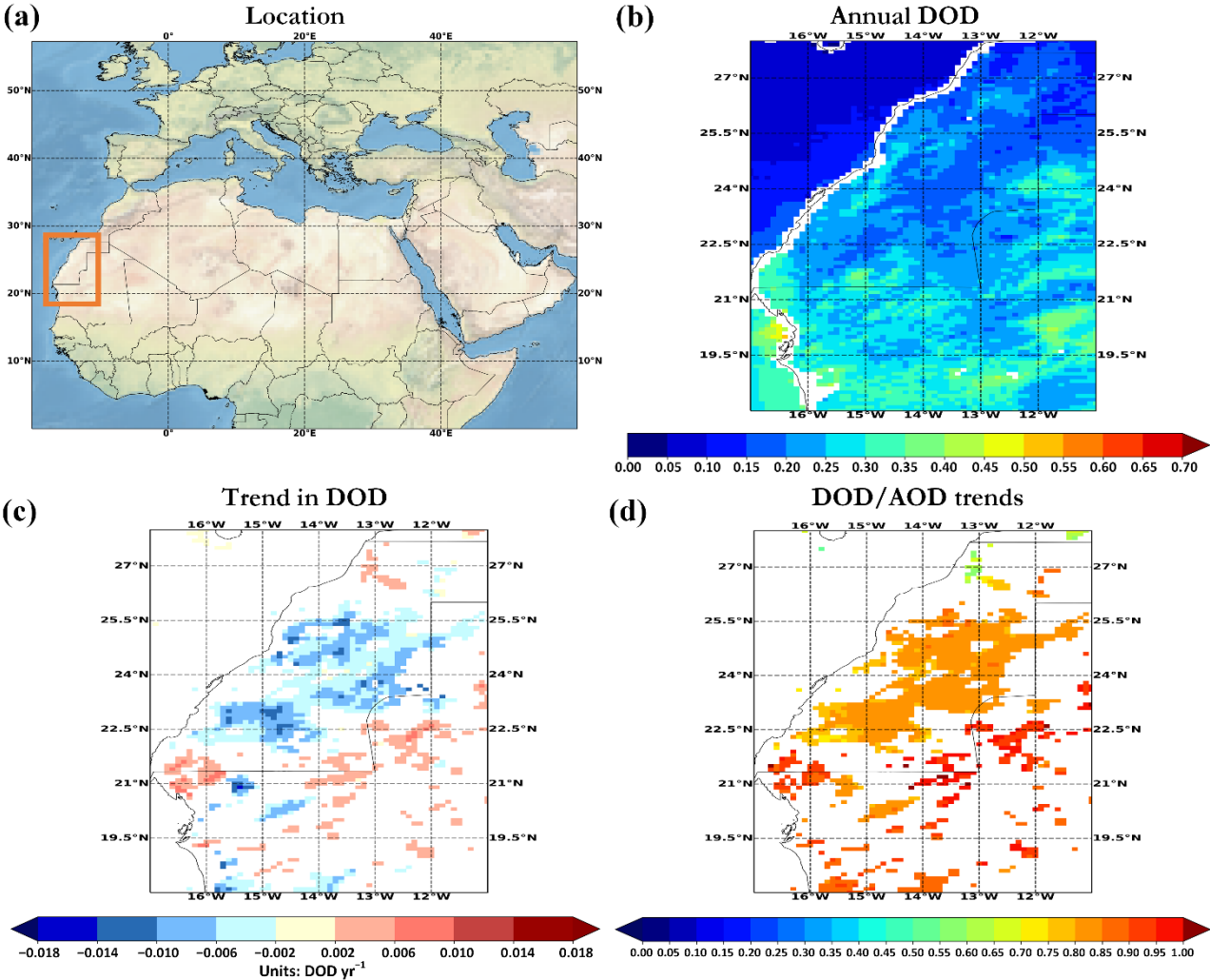
Figure 11: Same as Fig. 10, but for the Western Sahara.

563   In the eastern sector of the Sahara Desert (ESA), statistically significant negative DOD trends (down to −0.023 yr⁻¹) (Fig.
564   12c) are revealed as well as both for regional DOD (Fig. 8a) and AOD (Fig. 8b) trend thus indicating the predominant
565   contribution of mineral particles to the total aerosol load. Reduction of the dust burden has also been recorded from
566   MODIS/Terra dataset according to Voss and Evan (2020). Dust particles affect potentially total AOD across ESA indicating
567   a regional DOD to AOD trend ratio of 1.06. Over the dust-affected areas of the planet, the DOD to AOD trends ratio range
568   from negative (different trend sign) to higher than unity values. Since the dust burden modulate the total AOD over 'dusty'
569   regions, the ratio between DOD and AOD is expected around unity. Higher ratios than unity are expected as the non-dust AOD
570   signal decreases or increases and the DOD signal shows a reciprocal pattern. According to Fig. 9, two significant outcomes
571   can be extracted in ESA. The magnitude, in absolute terms, of the decreasing DOD trends increases (down to −0.0054 yr⁻¹;
572   2012−2017) and the statistical significance is achieved for shorter time periods for increasing starting years.
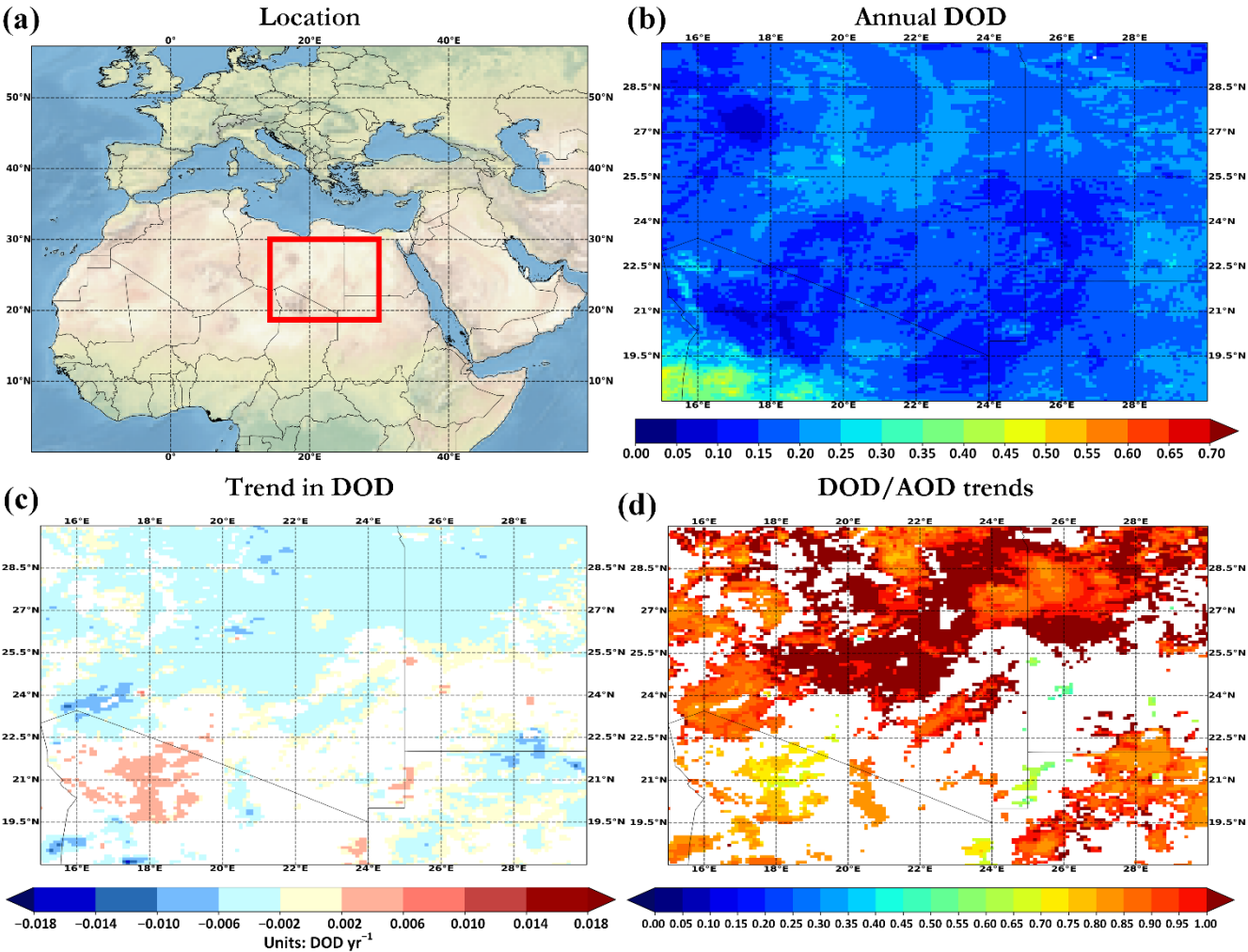
573

574 **Figure 12: Same as Fig. 10, but for the Eastern Sahara.**

575   Within the study period, the regional dust load decreases (-0.0055 yr^{-1}) in the Bodélé Depression (BOD) consisting the

576 most active aeolian dust source of the planet (Prospero et al., 2002; Washington et al., 2006; Todd et al., 2007; Gkikas et al.,

577 2021b). DOD trends range from -0.021 yr^{-1} to -0.003 yr^{-1} (Fig. 13c), corroborating the findings of the Voss and Evan (2020).

578 For starting years between $2003-2010$ the dust aerosol burden decreases (Fig. 9), with the most negative trend found during

579 $2007-2014$ (-0.015 yr^{-1}). As the starting year increases and the time length decreases, the magnitude of DOD trends become

580 weaker. More specifically, the sign of DOD trends is shifted using $2011-2013$ as starting years, but the results are not

581 statistically significant. The latter indicates that DOD over the most active dust source of the planet becomes more intense

582 during the last years. The aerosols' burden over the Sahara Desert is modulated by meteorological parameters affecting the

583 dust emissions such as precipitation (Pozzer et al., 2015) and wind speed (Che et al., 2019). Based on model simulations,

584 Pozzer et al. (2015) confirmed that positive AOD trends across Sahara Desert are linked to negative precipitation trends during

585 2001-2010. Decreasing precipitation levels reduces dust deposition and favors dust transport, leading to an increase in dust

586 amounts. In addition, Che et al. (2019) reported that wind speed is the most critical feature for explaining the variance of AOD

587 (by 29.8%). During the high dust seasons, the interannual variation of dust emissions is affected by wind speed and the NLLJ

588 (in the southern Sahara dust sources) as well as by the Harmattan surge and Mediterranean depressions (in the northern Sahara

589 dust sources) (Shi et al., 2021).
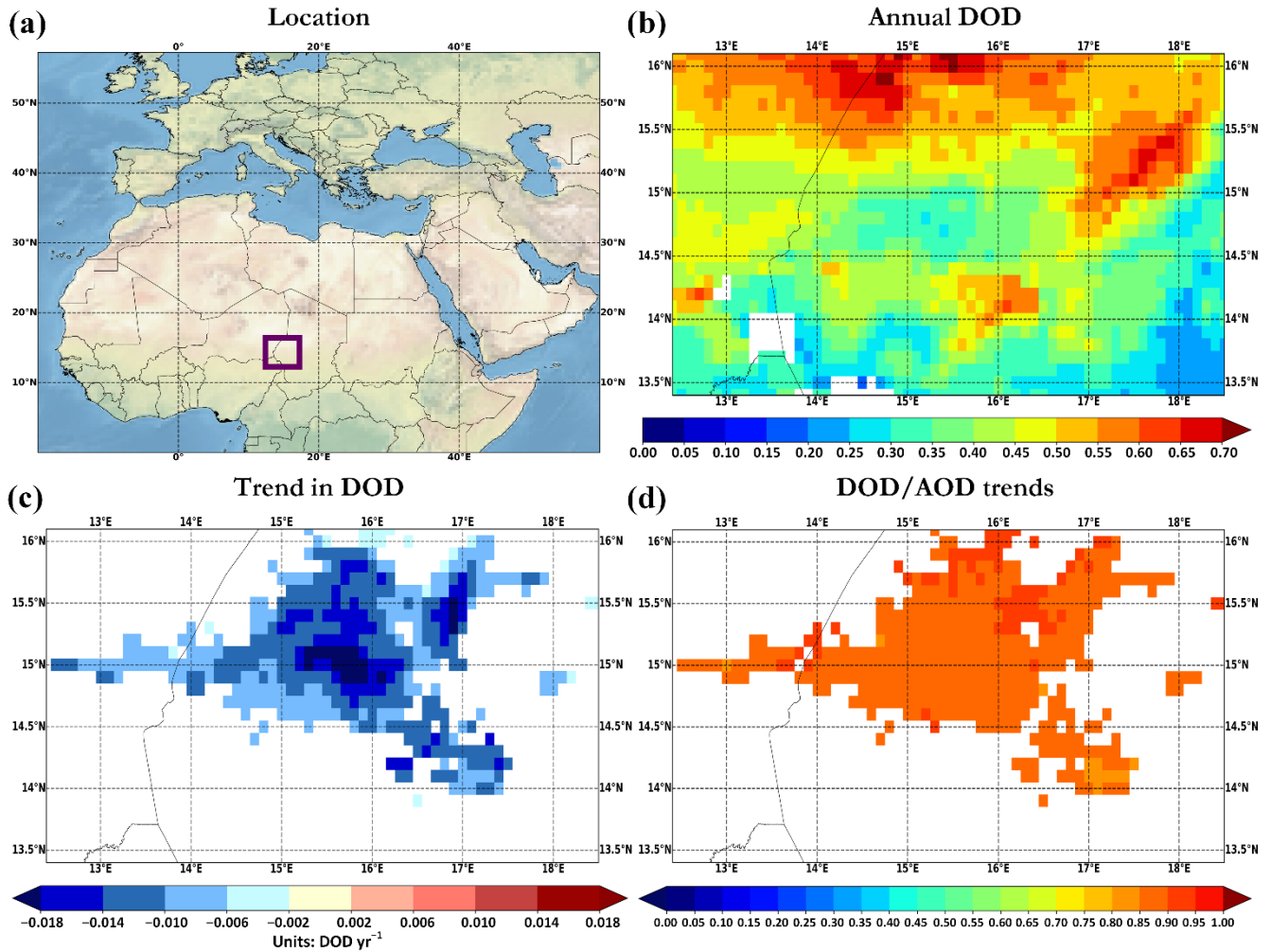
Figure 13: Same as Fig. 10, but for the Bodélé Depression.

3.3.3 Arabian Peninsula

The DOD tendencies over the Arabian Peninsula are presented separately for the northern (NAP) and the southern (SAP; including Jordan, Iraq and Syria) sectors. In both regions, positive trends (non-significant, Fig. 8a) are computed which are stronger in the southern parts of the Arabian Peninsula.

North Arabian Peninsula - NAP

(a) Location

(b) Annual DOD

(c) Trend in DOD

(d) DOD/AOD trends
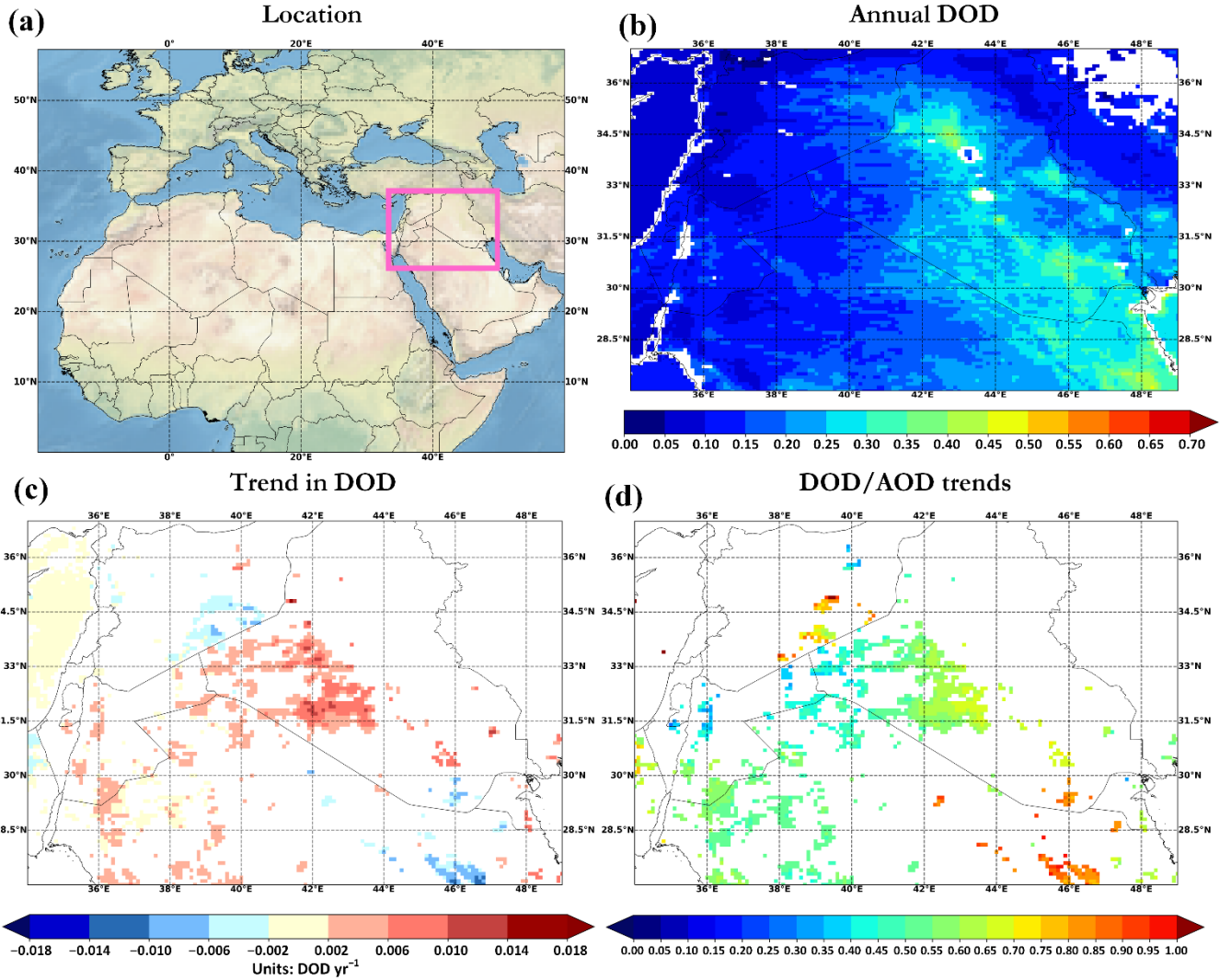
Figure 14: Same as Fig. 10, but for the North Arabian Peninsula.

Across Arabian Peninsula, the sign of the trend provides a bimodal pattern, revealing strong positive trends for time frames up to 2013 and followed by negative trends onwards (Fig. 9). Our findings are consistent with the revealed regime shift regarding dust activity in the Arabian Peninsula, as discussed in Notaro et al. (2015). The increased dust activity is also reflected in MIDAS DODs between 2008 and 2012, recording increased and stable annual DOD values (~0.2) compared to the previous 2003−2007 period DOD values (~0.15). Due to these sudden changes of dust amounts tendencies (from positive to negative), the regional DOD trends revealed non-significant within the entire study period (Fig. 8a). Klingmüller et al. (2016) documented increasing AOD trends during 2001−2012 followed by declining tendencies onwards, in agreement with our findings (Fig. 9). The predominant role of mineral particles on the total aerosol load across the Arabian Peninsula, is also

606 reflected by the moderate-to-high DOD/AOD trend ratios (up to 0.65; Figs. 14d and 15d). Both increases in DOD and non-

607 dust AOD explain the moderate in magnitude trend ratios.

608

609
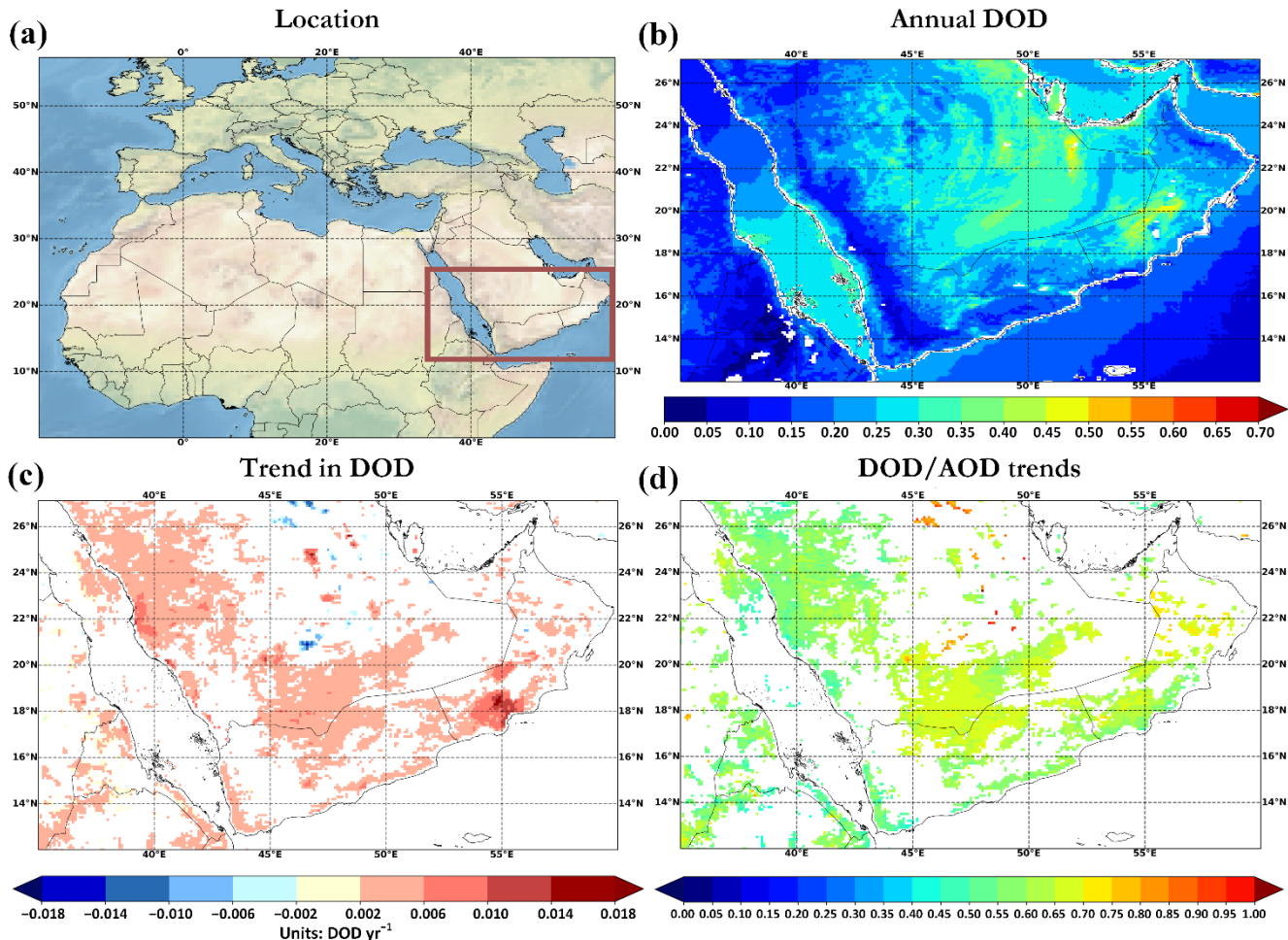
610 **Figure 15: Same as Fig. 10, but for the South Arabian Peninsula.**

611 In the last few decades, compelling inter-annual dust activity is documented in the Arabian Peninsula (Notaro et al., 2015).

612 Numerous studies examined the temporal variability of aerosol loads in the Middle East, showing strong ascending tendencies

613 (de Meij et al., 2012; Hsu et al., 2012; Yoon et al., 2014; Pozzer et al., 2015; Klingmüller et al., 2016; Che et al., 2019; Wei et

614 al., 2019a). Klingmüller et al. (2016) revealed that the positive AOD trends in Middle East are associated with decreasing

615 trends of Ångström exponent (AE) and fine mode fraction (FMF) indicating a shift towards a regime with stronger presence

616 of coarse particles. These findings are in agreement with the increasing DOD trends documented in this study during the same

617 study period (Fig. 9). Moreover, Klingmüller et al. (2016) implemented a multivariate linear model for annual AOD in order

618   to identify the linkage of AOD trends with critical parameters such as the precipitation, the surface soil moisture and the surface

619   wind speed. Soil moisture is the major controlling parameter in Saudi Arabia and Iraq whereas precipitation dominates in Iran.

620   For all regions, the addition of surface wind speed as independent parameter upgraded the model performance. Moreover, Che

621   et al. (2019) also used a multiple linear regression model to investigate the relationship of AOD with specific meteorological

622   parameters. The most appropriate ones, in terms of statistical significance, are chosen to enhance the model performance.

623   Across Middle East, the major controlling meteorological parameter for AOD variance is the sea level pressure (60.9% of total

624   AOD explained variation) and the wind speed, highlighting the large impact of synoptic systems on dust burden over the area.

625

3.3.4 Mediterranean

627   The Mediterranean (MED) basin is a region of great concern due to high inter-annual variability of aerosol loadings and

628   types (Floutsi et al., 2016). In this study, MED presents significant DOD trends ranging from -0.009 yr^{-1} to 0.006 yr^{-1} (Fig.

629   16c). The regional analysis documents strong declining significant DOD (Fig. 8a) and AOD (Fig. 8b) tendencies across the

630   MED basin. Negative DOD trends are also revealed during different sub-periods (Fig. 9). The DOD to AOD trends ratio shows

631   a latitudinal reduction moving from northern African coasts to the northern parts of the Mediterranean (Fig. 16d). Higher ratio

632   values are documented in South Mediterranean-North African coast region (0.3-1.94, median = 0.71) (Lat: 30.0−38.0 ºN; Lon:

633   6.0 ºW−30.0 ºE) compared to North Mediterranean (0.21-0.91, median = 0.45) (Lat: 38.0−45.0 ºN; Lon: 1.0 ºW−27.0 ºE). Dust

634   particles originated from North African and Middle East deserts driven by low pressure systems (cyclones) can be transported

635   towards MED (Gkikas et al., 2015), providing relatively high AOD values at the southern parts. Mineral particles are recorded

636   mainly in summer, spring and winter in Western, Central and East MED, respectively (Floutsi et al., 2016; Gkikas et al., 2013;

637   2016; 2021b). Across the north sector of MED, lower AOD values are associated with higher FMF values due to the prevailing

638   anthropogenic fine aerosols (Floutsi et al., 2016). The latter could also be observed from the negligible DOD trends there (Fig.

639   16c).
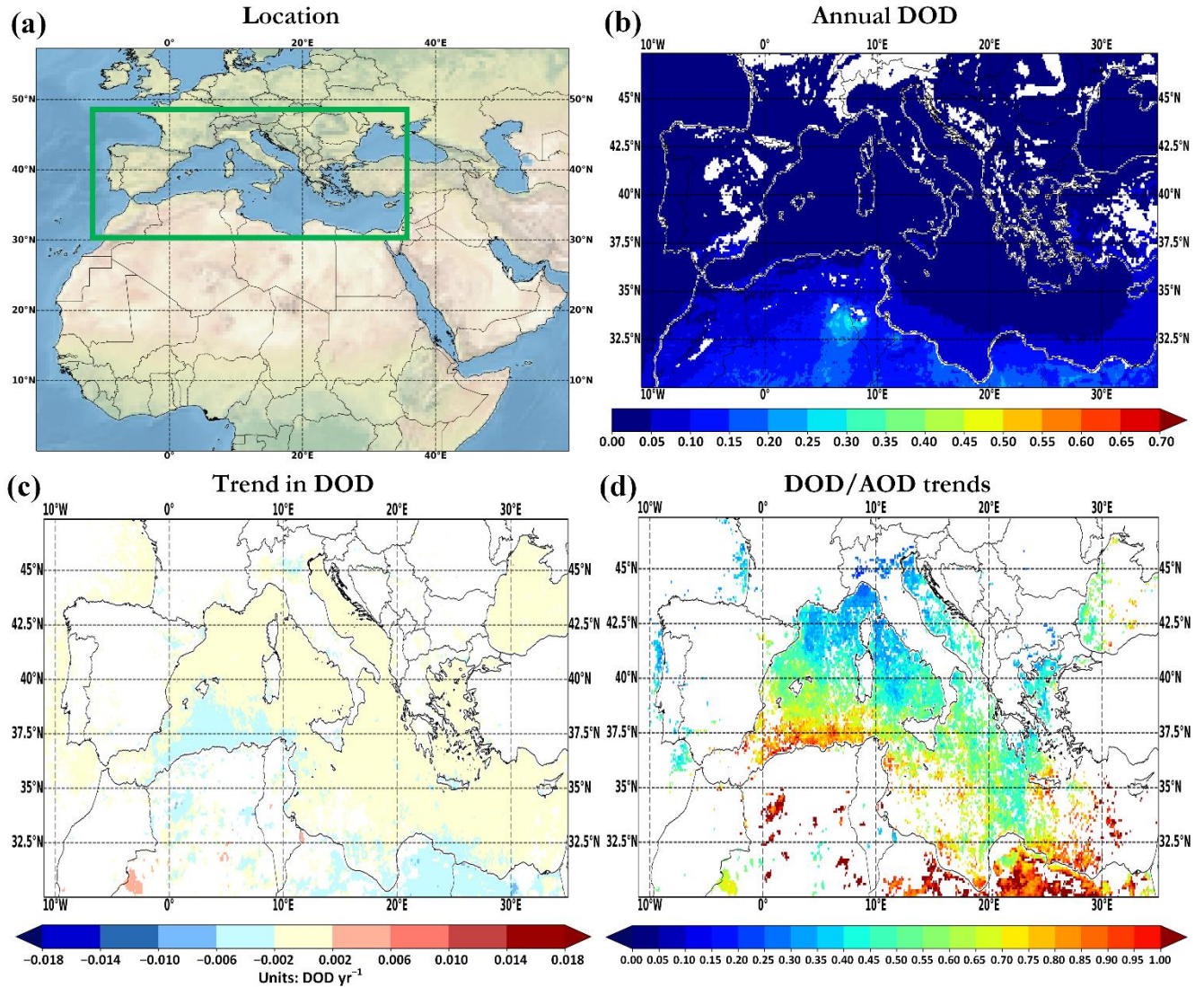
Figure 16: Same as Fig. 10, but for the Mediterranean Basin.

Earlier studies investigated the temporal AOD variability in the broader Mediterranean basin, reporting declining tendencies for the last two decades (Papadimas et al., 2008; de Meij et al., 2012; Hsu et al., 2012; Yoon et al., 2014; Pozzer et al., 2015; Floutsi et al., 2016; Che et al., 2019). Across this region, Floutsi et al. (2016) reported significant decreasing AOD trends of -0.0030 yr^{-1} over the period 2002−2014. Additionally, Nabat et al, 2013, reported decreasing DOD trends (-0.0045 yr^{-1}) across northern Africa. Both studies corroborate with the findings of this study where the overwhelming majority DOD trends are primarily slightly negative (Fig. 16c).

3.3.5 Thar and Gobi Deserts

Across the western part of Indo-Gangetic Plain, in the northwest area of the Indian Subcontinent, the Thar Desert (THA) is situated. THA region depicts significant decreasing DOD trends (down to -0.017 yr^{-1}) (Fig. 17c) modulating the corresponding declining AOD tendencies as indicated by the relatively high DOD/AOD trends ratio (0.67; Fig. 17d). The statistical significance of DOD trends, which are always negative regardless the sub-period, is strongly affected by the starting year as well as the length of the time interval in which the tendencies are computed (Fig. 9). More specifically, negative and not statistically significant DOD trends are observed for all time periods beginning from 2005. During the last two decades, strong negative temporal trends are recorded for OMI ultraviolet aerosol index (Hammer et al., 2018) along with AOD (Che et al., 2019) and DOD (Voss and Evan, 2020) across THA. The reduction of dust abundance over THA is mainly attributed to the increase of the rainfall and soil moisture enhancing wet dust deposition and reducing dust erosion during pre-monsoon (Pandey et al., 2017; Jin and Wang, 2018).
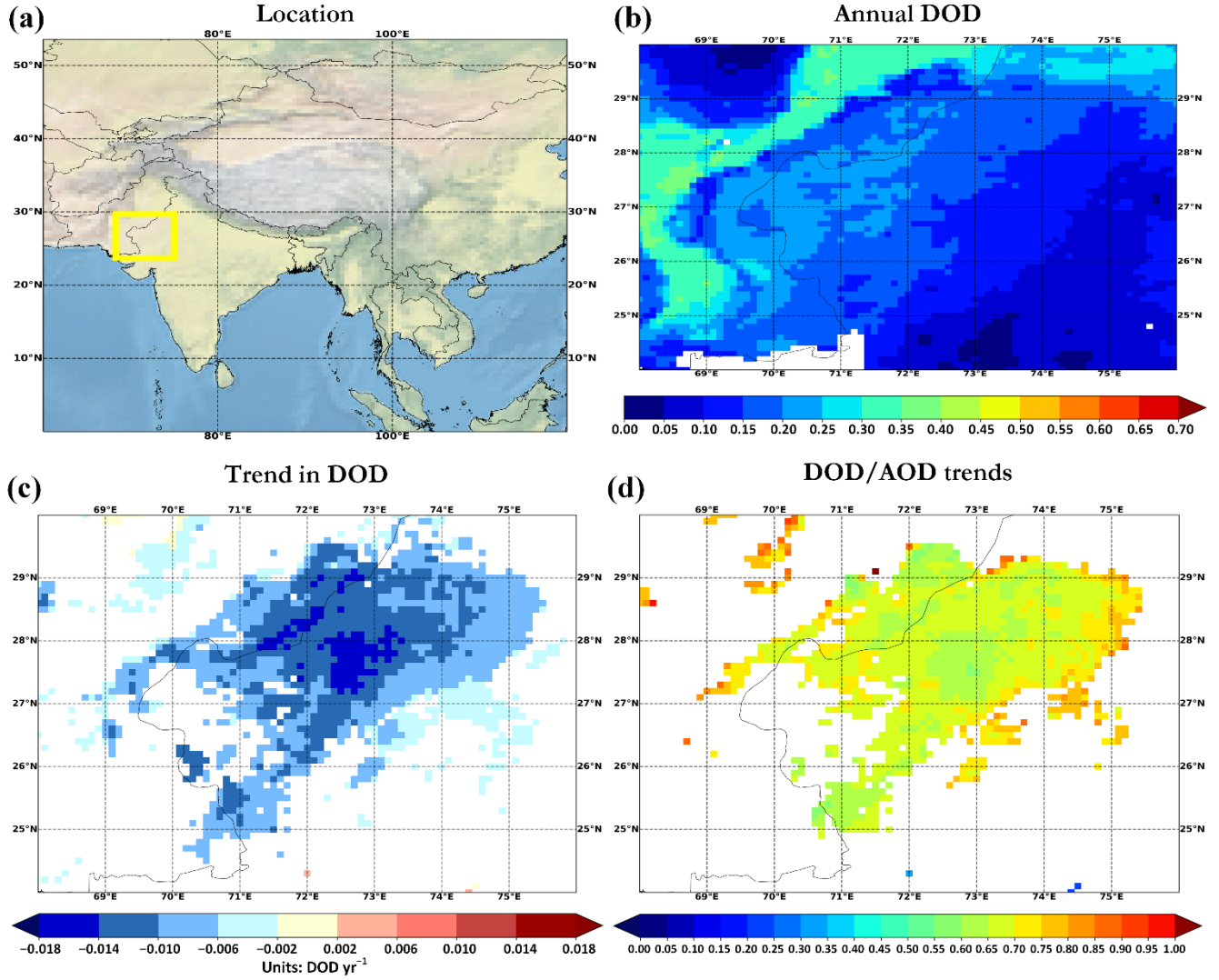
Figure 17: Same as Fig. 10, but for the Thar Desert.

The Gobi Desert (GOB) resides between the north part of China and the southern sector of Mongolia (East Asia). In this region, statistically significant DOD trends, ranging from -0.011 yr^{-1} to 0.004 yr^{-1}, are reported (Fig. 18c), in agreement (both in sign and magnitude) with those reported by Che et al. (2019) and Voss and Evan (2020) for AOD and DOD, respectively. At a regional level, slightly negative DOD (-0.00071 yr^{-1}) and AOD (-0.0010 yr^{-1}) trends, and statistically significant at 90% confidence level ($|\omega/\sigma_{\omega}|>1.65$), are computed (Fig. 8). Nevertheless, for time periods onwards 2005, the DOD trends are statistically significant at 95% confidence level (Fig. 9). These temporal DOD trends corroborate with Filonchyk et al. (2019), who computed AOD trends equal to -0.004 decade^{-1} and -0.002 decade^{-1} for MODIS/Terra and MISR measurements,

668 respectively, over the period 2000−2017. In addition, GOB AOD trends are strongly influenced by the presence of dust

669 particles, recording moderate median DOD to AOD trends ratio value of 0.62 (Fig. 18d).

670
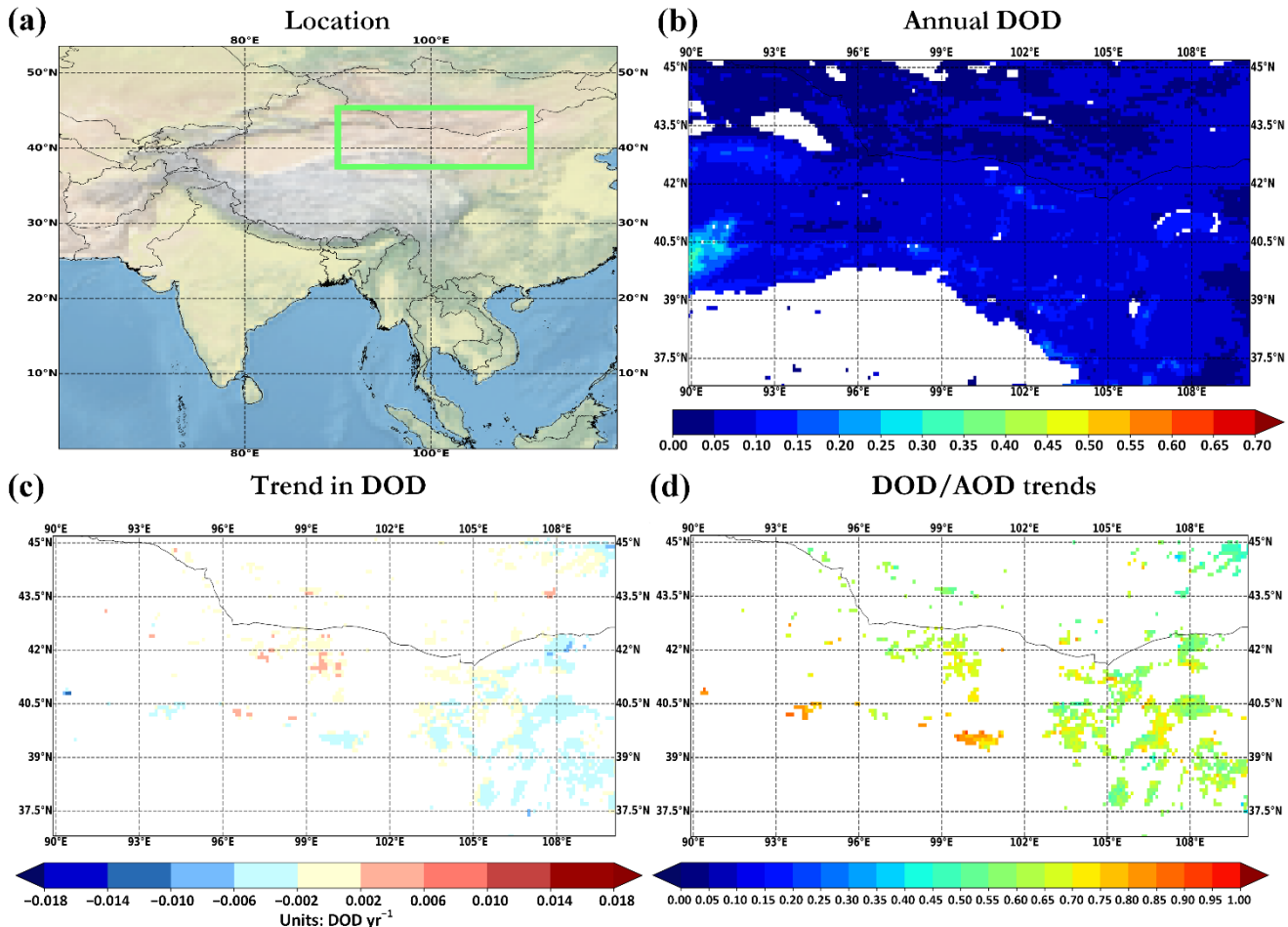
671 **Figure 18: Same as Fig. 10, but for the Gobi Desert.**

672 An et al. (2018) conducted a comprehensive analysis to investigate the potential factors driving the reduction of sand and

673 dust storms, taking place mainly in springtime, in East Asia between 2006 and 2017. In the aforementioned study, across GOB,

674 the mean surface dust concentration was declined by −31.71 $\mu g \ m^{-3} \ yr^{-1}$ (−12.24 %). These declining trends are regulated by

675 changes in the surface conditions (e.g. vegetation coverage) which are strongly linked to precipitation, soil moisture, ambient

676 temperature and human activities. The increasing trends in vegetation coverage are observed using the Normalized Difference

677 Vegetation Index (NDVI) (0.0006 yr^{-1}) from MODIS and are linked with the ascending tendencies of the precipitation (0.002

678 mm $day^{-1} \ yr^{-1}$) and volumetric soil moisture at 0-0.1 m depth (0.316 yr^{-1}). All these factors converge towards the reduction of

679 emitted amounts of dust aerosols. Over East Asia, the frequency and intensity of dust outbreaks have been decreased during

the springtime (An et al., 2018). Dust particles are primarily uplifted into the surrounding air across this region due to massive winds accompanied by cold air from northern latitudes. The decreasing frequency and intensity of dust outbreaks can be explained by the declining tendencies of the north wind components, documented during 2007−2016. The latter is associated with the decline of 1) Polar Vortex intensity, 2) north-to-south mean surface level pressure gradient and 3) meridional wind component magnitude.

4 Summary and conclusions

Airborne dust affects the global and regional climate via the induced perturbation of the solar and terrestrial radiation fields. Therefore, the investigation of DOD temporal variations is crucial to assess its climatic role as well as the multifarious impacts within the Earth-Atmosphere system and humans' health. The present study deals with the investigation of the annual and seasonal trends of AOD and DOD, both at global and regional scales over the period 2003–2017, relying on the MIDAS fine resolution dataset. Taking advantage of the MIDAS strong capabilities, the DOD trends have been analyzed: (i) by considering different aggregation approaches (i.e. arithmetic and geometric means), (ii) at fine and coarse spatial resolutions, (iii) applying and not applying temporal filters (iv) at annual, seasonal and sub-period time scales (i.e. sliding window) and (v) their contribution to the corresponding tendencies of the total aerosol optical depth. Based on this holistic approach, it is provided a complete overview about the temporal variability of dust loads addressing jointly all the factors determining the sign, the magnitude and the statistical significance of the calculated trends.

The validity of the MIDAS DOD trends has been investigated with respect to AERONET cAOD data. This analysis encompassed that MIDAS tendencies are capable to follow those of AERONET either for increasing (at 26 out of 30 stations, 86.7%) or decreasing (at 7 out of 11 stations, 63.6%) trends. Point-to-point investigation of the DOD-cAOD trends highlighted the accurate, in terms of magnitude and statistical significance, MIDAS DOD trends either across "dusty" sites or downwind areas.

The sensitivity analysis between coarse and fine spatial resolution revealed that the magnitude of AOD and DOD trends are lower for the coarse spatial resolution data. On a regional basis, the calculated AOD/DOD trends revealed a very good agreement in terms of trend magnitude for both spatial scales. In general, coarse resolution data provide better spatial coverage, however, detailed information, in spatial terms, is when fine resolution data are utilized. In addition, the sensitivity analysis on the different aggregation approaches revealed that the arithmetic-based trends are larger than those of the geometric-based ones (from 52.87 to 91.77%) all over the globe. The only exception was found only for AOD at coarse spatial resolution. Lastly, the sensitivity analysis on the temporal filtering in trend calculations indicated new regions (e.g. across oceanic territories) with unphysical unfiltered AOD trends. In addition, unfiltered trends led to poorer performance of MIDAS DOD trends against AERONET retrievals.

Based on our analysis, increasing DOD trends are obtained across the Central Sahara and the Arabian Peninsula whereas opposite tendencies are recorded over the Eastern and Western Sahara, the Thar and Gobi Deserts, in the Bodélé Depression

and in southern Mediterranean. On the seasonal basis, the maximum positive DOD trends are displayed in the Central Sahara and Middle East area during summertime. During spring, the strongest reductions of the dust burden have been revealed at the Bodélé Depression whereas reverse tendencies have been recorded in the Western and Eastern Sahara and in the Thar and Taklamakan Deserts during summer. Similarly, the most negative trends were observed at spring over the Gobi Desert. Positive trends across the area extending from North Atlantic Ocean to the eastern Caribbean Sea are observed in spring.

At global scale and separately over continents and oceans, negligible and non-significant DOD trends are found. A similar analysis for 9 specific regions of the planet has been performed revealing evident trends which are not however all of them statistically significant. More specifically, strong DOD trends were documented in Central (0.0021 yr^{-1}) and East (-0.0018 yr^{-1}) Sahara, Bodélé Depression (-0.0055 yr^{-1}), Mediterranean (-0.0011 yr^{-1}) and Thar Desert (-0.0053 yr^{-1}). In contrast, non-significant regional DOD trends were depicted in the Arabian Peninsula and the Gobi Desert. At a regional scale, the calculated trends vary in terms of sign, magnitude and statistical significance, depending on the sub-period, thus indicating a strong interannual variation of dust aerosols' load within the period 2003–2017. In the majority of the regions of interest, including also downwind areas, the variations of the total aerosol load are driven by those of mineral particles.

The obtained findings from the current study highlight the applicability of the MIDAS dataset for detecting dust temporal across various spatial scales. The high spatiotemporal resolution of MIDAS provides the opportunity to complement and further expand the existing knowledge on this critical aspect, yet not well covered in the field of dust research. Likewise, by comparing AOD and DOD tendencies, it is feasible the assessment of mineral particles' role on the variations of the total aerosol load. Our results could be incorporated in chemical models, either for assessing the various impacts of dust and non-dust particles or for evaluating trends based on numerical simulations, and to further improve their calibration and forecast performance. Moreover, the obtained findings here can be used for the interpretation of the trends of the radiation fluxes at the surface and at the top of the atmosphere obtained by observations or atmospheric-aerosol models (Chaibou et al., 2020). The recently published Sixth Assessment Report (AR6) of the Intergovernmental Panel on Climate Change (IPCC) states that the increase of the global dust load causes a reduction of the effective radiative forcing (ERF) by -0.25 Wm^{-2} (Andrews et al., 2017; Forster et al., 2021). Therefore, fluctuations of the dust atmospheric load provide a valuable information in order to understand the associated impacts on past, current and future climate. Finally, the current study focused mainly on the description of dust optical depth trends providing also a preliminary interpretation of the obtained findings. Nevertheless, an in-depth analysis (a follow up study) is ongoing by investigating the role of critical meteorological variables (e.g. wind) as well as of other determinant geophysical factors (e.g. soil moisture, vegetation, land coverage) on the configuration of DOD trends.

Acknowledgments

We acknowledge support of this work by the project "PANhellenic infrastructure for Atmospheric Composition and climatE change" (MIS 5021516) which is implemented under the Action "*Reinforcement of the Research and Innovation*

744 *Infrastructure*", funded by the Operational Programme "Competitiveness, Entrepreneurship and Innovation" (NSRF 2014-

745 2020) and co-financed by Greece and the European Union (European Regional Development Fund). The MIDAS dataset has

746 been developed in the framework of the DUST-GLASS project (grant no. 749461; European Union's Horizon 2020 Research

747 and Innovation programme under the Marie Skłodowska-Curie Actions. Antonis Gkikas acknowledges support by the Hellenic

748 Foundation for Research and Innovation (H.F.R.I.) under the "2nd Call for H.F.R.I. Research Projects to support Post-Doctoral

749 Researchers" (Project Acronym: ATLANTAS, Project number: 544). Vassilis Amiridis acknowledges support from the

750 European Research Council (grant no. 725698; D-TECT). Stelios Kazadzis acknowledges the International Network to

751 Encourage the Use of Monitoring and Forecasting Dust Products (inDust) COST Action CA16202. We gratefully acknowledge

752 the data provided by AERONET network and we wish to express our appreciation to the operators of stations for their efforts

753 on running the instruments.

754 **Author contribution**

755 SAL was responsible for the whole analysis and the preparation of the initial manuscript with support from VS. AG processed

756 the MIDAS dataset and had an advisory role in the relevant parts of the study. AK and SK conceptualized the main objective

757 of the manuscript and supervised the progress. VA provided feedback on the scientific discussions. All authors contributed to

758 the revision and the final editing of the initial manuscript.

759 **Competing interests**

760 The authors declare that they have no competing interests.

761 **References**

762 Adesina, A. J., Kumar, K. R., Sivakumar, V. and Piketh, S. J.: Intercomparison and assessment of long-term (2004–2013)

763 multiple satellite aerosol products over two contrasting sites in South Africa, J. Atmos. Solar-Terrestrial Phys., 148, 82–95,

764 https://doi.org/10.1016/j.jastp.2016.09.001, 2016.

765 Alfaro-Contreras, R., Zhang, J., Reid, J. S. and Christopher, S.: A study of 15-year aerosol optical thickness and direct

766 shortwave aerosol radiative effect trends using MODIS, MISR, CALIOP and CERES, Atmos. Chem. Phys., 17(22), 13849–

767 13868, https://doi.org/10.5194/acp-17-13849-2017, 2017.

768 Alizadeh-Choobari, O., Zawar-Reza, P., Sturman, A.: The global distribution of mineral dust and its impacts on the climate

769 system: A review, Atmos. Res., 138, 152–165, 1174, https://doi.org/10.1016/j.atmosres.2013.11.007, 2014a.

770 Alizadeh-Choobari, O., Zawar-Reza, P., Sturman, A.: The "wind of 120 days" and dust storm activity over the Sistan
771 Basin, Atmos. Res., 143, 328–341, https://doi.org/10.1016/j.atmosres.2014.02.001, 2014b.

772 Alizadeh-Choobari, O., Sturman, A. and Zawar-Reza, P.: A global satellite view of the seasonal distribution of mineral dust
773 and its correlation with atmospheric circulation, Dyn. Atmos. Ocean., 68, 20–34,
774 https://doi.org/10.1016/j.dynatmoce.2014.07.002, 2014c.

775 Amiridis, V., Wandinger, U., Marinou, E., Giannakaki, E., Tsekeri, A., Basart, S., Kazadzis, S., Gkikas, A., Taylor, M.,
776 Baldasano, J., and Ansmann, A.: Optimizing CALIPSO Saharan dust retrievals, Atmos. Chem. Phys., 13, 12089–12106,
777 https://doi.org/10.5194/acp-13-12089-2013, 2013.

778 Amiridis, V., Marinou, E., Tsekeri, A., Wandinger, U., Schwarz, A., Giannakaki, E., Mamouri, R., Kokkalis, P., Binietoglou,
779 I., Solomos, S., Herekakis, T., Kazadzis, S., Gerasopoulos, E., Proestakis, E., Kottas, M., Balis, D., Papayannis, A., Kontoes,
780 C., Kourtidis, K., Papagiannopoulos, N., Mona, L., Pappalardo, G., Le Rille, O., and Ansmann, A.: LIVAS: a 3-D multi-
781 wavelength aerosol/cloud database based on CALIPSO and EARLINET, Atmos. Chem. Phys., 15, 7127–7153,
782 https://doi.org/10.5194/acp15-7127-2015, 2015.

783 An, L., Che, H., Xue, M., Zhang, T., Wang, H., Wang, Y., Zhou, C., Zhao, H., Gui, K., Zheng, Y., Sun, T., Liang, Y., Sun, E.,
784 Zhang, H. and Zhang, X.: Temporal and spatial variations in sand and dust storm events in East Asia from 2007 to 2016:
785 Relationships with surface conditions and climate change, Sci. Total Environ., 633, 452–462,
786 https://doi.org/10.1016/j.scitotenv.2018.03.068, 2018.

787 Andrews, T., Betts, R. A., Booth, B. B. B., Jones, C. D., and Jones, G. S.: Effective radiative forcing from historical land use
788 change, Clim. Dynam., 48, 3489–3505, https://doi.org/10.1007/s00382-016-3280-7, 2017.

789 Babu, S. S., Manoj, M. R., Moorthy, K. K., Gogoi, M. M., Nair, V. S., Kompalli, S. K., Satheesh, S. K., Niranjan, K.,
790 Ramagopal, K., Bhuyan, P. K. and Singh, D.: Trends in aerosol optical depth over Indian region: Potential causes and impact
791 indicators, J. Geophys. Res. Atmos., 118(20), 11,794-11,806, https://doi.org/10.1002/2013JD020507, 2013.

792 Basart, S., Pérez, C., Cuevas, E., Baldasano, J. M., and Gobbi, G. P.: Aerosol characterization in Northern Africa, Northeastern
793 Atlantic, Mediterranean Basin and Middle East from direct-sun AERONET observations, Atmos. Chem. Phys., 9, 8265–8282,
794 https://doi.org/10.5194/acp-9-8265-2009, 2009.

795 Chaibou, A. A. S., Ma, X., and Sha, T.: Dust radiative forcing and its impact on surface energy budget over West Africa,
796 Scientific Reports, 10, https://doi.org/10.1038/s41598-020-69223-4, 2020.

797 Che, H., Qi, B., Zhao, H., Xia, X., Eck, T. F., Goloub, P., Dubovik, O., Estelles, V., Cuevas-Agulló, E., Blarel, L., Wu, Y.,
798 Zhu, J., Du, R., Wang, Y., Wang, H., Gui, K., Yu, J., Zheng, Y., Sun, T., Chen, Q., Shi, G., and Zhang, X.: Aerosol optical
799 properties and direct radiative forcing based on measurements from the China Aerosol Remote Sensing Network (CARSNET)
800 in eastern China, Atmos. Chem. Phys., 18, 405–425, https://doi.org/10.5194/acp-18-405-2018, 2018.

801 Che, H., Gui, K., Xia, X., Wang, Y., Holben, B. N., Goloub, P., Cuevas-Agulló, E., Wang, H., Zheng, Y., Zhao, H., and Zhang,
802 X.: Large contribution of meteorological factors to inter-decadal changes in regional aerosol optical depth, Atmos. Chem.
803 Phys., 19, 10497–10523, https://doi.org/10.5194/acp-19-10497-2019, 2019.

804 Chen, J. L., Pekker, T., Wilson, C. R., Tapley, B. D., Kostianoy, A. G., Cretaux, J. F. and Safarov, E. S.: Long-term Caspian
805 Sea level change, Geophys. Res. Lett., 44(13), 6993–7001, https://doi.org/10.1002/2017GL073958, 2017.

806 Clarisse, L., Clerbaux, C., Franco, B., Hadji-Lazaro, J., Whitburn, S., Kopp, A. K., Hurtmans, D., and Coheur, P.-F.: A Decadal
807 Data Set of Global Atmospheric Dust Retrieved From IASI Satellite Measurements, J. Geophys. Res.-Atmos., 124, 1618–
808 1647, https://doi.org/10.1029/2018JD029701, 2019.

809 Dahutia, P., Pathak, B., and Bhuyan, P. K.: Aerosols characteristics, trends and their climatic implications over Northeast India
810 and adjoining South Asia, Int. J. Climatol., 38, 1234–1256, https://doi.org/10.1002/joc.5240, 2017.

811 de Meij, A., Pozzer, A. and Lelieveld, J.: Trend analysis in aerosol optical depths and pollutant emission estimates between
812 2000 and 2009, Atmos. Environ., 51, 75–85, https://doi.org/10.1016/j.atmosenv.2012.01.059, 2012.

813 Dubovik, O. and King, M. D.: A flexible inversion algorithm for retrieval of aerosol optical properties from Sun and sky
814 radiance measurements, J. Geophys. Res., 105, 20673–20696, https://doi.org/10.1029/2000JD900282, 2000.

815 Elguindi, N., Solmon, F., Turuncoglu, U.: Quantifying some of the impacts of dust and other aerosol on the Caspian Sea region
816 using a regional climate model. Clim. Dyn., 46, 41–55, https://doi.org/10.1007/s00382-015-2566-5, 2016.

817 Evan, A. T., Dunion, J., Foley, J. A., Heidinger, A. K., and Velden, C. S.: New evidence for a relationship between Atlantic
818 tropical   cyclone   activity   and   African   dust   outbreaks,   Geophysical   Research   Letters,   33,
819 https://doi.org/10.1029/2006GL026408, 2006.

820 Evan, A. T., Flamant, C., Gaetani, M., and Guichard, F.: The past, present and future of African dust, Nature, 531, 493–495,
821 https://doi.org/10.1038/nature17149, 2016.

822 Fréville, H., Chami, M. and Mallet, M.: Analysis of the Transport of Aerosols over the North Tropical Atlantic Ocean Using
823 Time Series of POLDER/PARASOL Satellite Data, Remote Sens., 12, 757, https://doi.org/10.3390/rs12050757, 2020.

824 Forster, P., Storelvmo, T., Armour, K., Collins, W., Dufresne, J. L., Frame, D., Lunt, D. J., Mauritsen, T., Palmer, M. D.,
825 Watanabe, M., Wild, M., Zhang H.: The Earth's Energy Budget, Climate Feedbacks, and Climate Sensitivity. In: Climate
826 Change 2021: The Physical Science Basis. Contribution of Working Group I to the Sixth Assessment Report of the
827 Intergovernmental Panel on Climate Change [Masson-Delmotte, V., P. Zhai, A. Pirani, S. L. Connors, C. Péan, S. Berger, N.
828 Caud, Y. Chen, L. Goldfarb, M. I. Gomis, M. Huang, K. Leitzell, E. Lonnoy, J. B. R. Matthews, T. K. Maycock, T. Waterfield,
829 O. Yelekçi, R. Yu and B. Zhou (eds.)]. Cambridge University Press. In Press, 2021.

830 Filonchyk, M., Yan, H., Zhang, Z., Yang, S., Li, W. and Li, Y.: Combined use of satellite and surface observations to study
831 aerosol optical depth in different regions of China, Sci. Rep., 9 (1), 1–15, doi:10.1038/s41598-019-42466-6, 2019.

832 Floutsi, A. A., Korras-Carraca, M. B., Matsoukas, C., Hatzianastassiou, N. and Biskos, G.: Climatology and trends of aerosol
833 optical depth over the Mediterranean basin during the last 12 years (2002-2014) based on Collection 006 MODIS-Aqua data,
834 Sci. Total Environ., 551–552, 292–303, https://doi.org/10.1016/j.scitotenv.2016.01.192, 2016.

835 Gelaro, R, McCarty, W., Suárez, M. J., Todling, R., Molod, A., Takacs, L., Randles, C. A., Darmenov, A., Bosilovich, M. G.,
836 Reichle, R., Wargan, K., Coy, L., Cullather, R., Draper, C., Akella, S., Buchard, V., Conaty, A., da Silva, A. M., Gu, W., Kim,
837 G., Koster, R., Lucchesi, R., Merkova, D., Nielsen, J. E., Partyka, G., Pawson, S., Putman, W., Rienecker, M., Schubert, S.
838 D., Sienkiewicz, M., and Zhao, B.: The Modern-Era Retrospective Analysis for Research and Applications, Version 2
839 (MERRA-2), J. Climate, 30, 5419–5454, https://doi.org/10.1175/JCLI-D-16-0758.1, 2017.

840 Giles, D. M., Holben, B. N., Eck, T. F., Sinyuk, A., Smirnov, A., Slutsker, I., Dickerson, R. R., and Thompson, A. M., and
841 Schafer, J. S.: An analysis of AERONET aerosol absorption properties and classifications representative of aerosol source
842 regions, J. Geophys. Res., 117, D17203, https://doi.org/10.1029/2012JD018127, 2012.

843 Giles, D. M., Sinyuk, A., Sorokin, M. G., Schafer, J. S., Smirnov, A., Slutsker, I., Eck, T. F., Holben, B. N., Lewis, J. R.,
844 Campbell, J. R., Welton, E. J., Korkin, S. V., and Lyapustin, A. I.: Advancements in the Aerosol Robotic Network
845 (AERONET) Version 3 database – automated near-real-time quality control algorithm with improved cloud screening for Sun
846 photometer aerosol optical depth (AOD) measurements, Atmos. Meas. Tech., 12, 169–209, https://doi.org/10.5194/amt-12-
847 169-2019, 2019.

848 Ginoux, P., Prospero, J. M., Gill, T. E., Hsu, N. C., and Zhao, M.: Global-scale attribution of anthropogenic and natural dust
849 sources and their emission rates based on MODIS Deep Blue aerosol products, Rev. Geophys., 50, RG3005,
850 https://doi.org/10.1029/2012RG000388, 2012.

851 Gkikas, A., Hatzianastassiou, N., Mihalopoulos, N., Katsoulis, V., Kazadzis, S., Pey, J., Querol, X., and Torres, O.: The regime
852 of intense desert dust episodes in the Mediterranean based on contemporary satellite observations and ground measurements,
853 Atmos. Chem. Phys., 13, 12135–12154, https://doi.org/10.5194/acp-13-12135-2013, 2013.

854 Gkikas, A., Houssos, E. E., Lolis, C. J., Bartzokas, A., Mihalopoulos, N., and Hatzianastassiou, N.: Atmospheric circulation
855 evolution related to desert-dust episodes over the Mediterranean, Q. J. Roy. Meteor. Soc., 141, 1634–1645,
856 https://doi.org/10.1002/qj.2466, 2015.

857 Gkikas, A., Basart, S., Hatzianastassiou, N., Marinou, E., Amiridis, V., Kazadzis, S., Pey, J., Querol, X., Jorba, O., Gassó, S.,
858 and Baldasano, J. M.: Mediterranean intense desert dust outbreaks and their vertical structure based on remote sensing data,
859 Atmos. Chem. Phys., 16, 8609–8642, https://doi.org/10.5194/acp-16-8609-2016, 2016.

860 Gkikas, A., Proestakis, E., Amiridis, V., Kazadzis, S., Di Tomaso, E., Tsekeri, A., Marinou, E., Hatzianastassiou, N., and Pérez
861 García-Pando, C.: ModIs Dust AeroSol (MIDAS): a global fine-resolution dust optical depth data set, Atmos. Meas. Tech.,
862 14, 309–334, https://doi.org/10.5194/amt-14-309-2021, 2021a.

863 Gkikas, A., Proestakis, E., Amiridis, V., Kazadzis, S., Di Tomaso, E., Marinou, E., Hatzianastassiou, N., Kok, J. F., and García-
864 Pando, C. P.: Quantification of the dust optical depth across spatiotemporal scales with the MIDAS global dataset (2003–
865 2017), Atmos. Chem. Phys. Discuss. [preprint], https://doi.org/10.5194/acp-2021-572, in review, 2021b.

866 Gläser, G., Wernli, H., Kerkweg, A., and Teubler, F.: The transatlantic dust transport from North Africa to the Americas-Its
867 characteristics and source regions, J. Geophys. Res.-Atmos., 120, 11231–11252, https://doi.org/10.1002/2015JD023792, 2015.

868 Goudie, A.S. and Middelton, N.J.: Desert Dust in the Global System, Springer, 2006.

869 Griffin, D. W., Kellogg, C. A., Garrison, V. H., and Shinn, E. A.: The global transport of dust. An intercontinental river of
870 dust, microorganisms and toxic chemicals flows through the Earth's atmosphere, Am. Sci., 90, 228–235, 2002.

871 Guo, J., Xu, H., Liu, L., Chen, D., Peng, Y., Yim, S. H. L., Yang, Y., Li, J., Zhao, C., and Zhai, P.: The trend reversal of dust
872 aerosol over East Asia and the North Pacific Ocean attributed to large-scale meteorology, deposition and soil moisture, J.
873 Geophys. Res.-Atmos., 124, 10450–10466, https://doi.org/10.1029/2019JD030654, 2019

874 Guo, J. P., Zhang, X. Y., Wu, Y. R., Zhaxi, Y., Che, H. Z., La, B., Wang, W. and Li, X. W.: Spatio-temporal variation trends
875 of satellite-based aerosol optical depth in China during 1980-2008, Atmos. Environ., 45(37), 6802–6811,
876 https://doi.org/10.1016/j.atmosenv.2011.03.068, 2011.

877 Hamill, P., Giordano, M., Ward, C., Giles, D., and Holben, B.: An AERONET-based aerosol classification using the
878 Mahalanobis distance, Atmos. Environ., 140, 213–233, https://doi.org/10.1016/j.atmosenv.2016.06.002, 2016.

879 Hammer, M. S., Martin, R. V., Li, C., Torres, O., Manning, M., and Boys, B. L.: Insight into global trends in aerosol
880 composition from 2005 to 2015 inferred from the OMI Ultraviolet Aerosol Index, Atmos. Chem. Phys., 18, 8097–8112,
881 https://doi.org/10.5194/acp-18-8097-2018, 2018.

882 Holben, B. N., Eck, T. F., Slutsker, I., Tanre, D., Buis, J. P., Setzer, A., Vermote, E., Reagan, J. A., Kaufman, Y., Nakajima,
883 T., Lavenue, F., Jankowiak, I., and Smirnov, A.: AERONET – A federated instrument network and data archive for aerosol
884 characterization, Remote Sens. Environ., 66, 1–16, https://doi.org/10.1016/S0034-4257(98)00031-5, 1998.

885 Hsu, N. C., Gautam, R., Sayer, A. M., Bettenhausen, C., Li, C., Jeong, M. J., Tsay, S.-C., and Holben, B. N.: Global and
886 regional trends of aerosol optical depth over land and ocean using SeaWiFS measurements from 1997 to 2010, Atmos. Chem.
887 Phys., 12, 8037–8053, https://doi.org/10.5194/acp-12-8037-2012, 2012.

888 Hu, K., Kumar, K. R., Kang, N., Boiyo, R. and Wu, J.: Spatiotemporal characteristics of aerosols and their trends over mainland
889 China with the recent Collection 6 MODIS and OMI satellite datasets, Environ. Sci. Pollut. Res., 25(7), 6909–6927,
890 https://doi.org/10.1007/s11356-017-0715-6, 2018.

891 Huang, J., Zhang, C., and Prospero, J. M.: African dust outbreaks: a satellite perspective of temporal and spatial variability
892 over the tropical Atlantic Ocean, J. Geophys. Res., 115, D05202, https://doi.org/10.1029/2009JD012516, 2010.

893 Jin, Q. and Wang, C.: The greening of Northwest Indian subcontinent and reduction of dust abundance resulting from Indian
894 summer monsoon revival, Sci. Rep., 8(1), 1–9, https://doi.org/10.1038/s41598-018-23055-5, 2018.

895 Kalashnikova, O. V. and Kahn, R. A.: Mineral dust plume evolution over the Atlantic from MISR and MODIS aerosol
896 retrievals, J. Geophys. Res., 113, D24204, https://doi.org/10.1029/2008JD010083, 2008.

897 Kaku, K. C., Reid, J. S., O'Neill, N. T., Quinn, P. K., Coffman, D. J., and Eck, T. F.: Verification and application of the
898 extended spectral deconvolution algorithm (SDA+) methodology to estimate aerosol fine and coarse mode extinction
899 coefficients in the marine boundary layer, Atmos. Meas. Tech., 7, 3399–3412, https://doi.org/10.5194/amt-7-3399-2014, 2014.

900   Klingmüller, K., Pozzer, A., Metzger, S., Stenchikov, G. L. and Lelieveld, J.: Aerosol optical depth trend over the Middle East,
901   Atmos. Chem. Phys., 16(8), 5063–5073, https://doi.org/10.5194/acp-16-5063-2016, 2016.

902   Kok, J. F., Ridley, D. A., Zhou, Q., Miller, R. L., Zhao, C., Heald, C. L., Ward, D. S., Albani, S., and Haustein, K.: Smaller
903   desert dust cooling effect estimated from analysis of dust size and abundance, Nat. Geosci., 10, 274–278,
904   https://doi.org/10.1038/ngeo2912, 2017.

905   Kumar, K. R., Yin, Y., Sivakumar, V., Kang, N., Yu, X., Diao, Y., Adesina, A. J. and Reddy, R. R.: Aerosol climatology and
906   discrimination of aerosol types retrieved from MODIS, MISR and OMI over Durban (29.88°S, 31.02°E), South Africa, Atmos.
907   Environ., 117, 9–18, https://doi.org/10.1016/j.atmosenv.2015.06.058, 2015.

908   Kumar, K. R., Boiyo, R., Madina, A. and Kang, N.: A 13-year climatological study on the variations of aerosol and cloud
909   properties over Kazakhstan from remotely sensed satellite observations, J. Atmos. Solar-Terrestrial Phys., 179, 55–68,
910   https://doi.org/10.1016/j.jastp.2018.06.014, 2018.

911   Lakshmi, N. B., Babu, S. S. and Nair, V. S.: Recent Regime Shifts in Mineral Dust Trends over South Asia from Long-Term
912   CALIPSO Observations, IEEE Trans. Geosci. Remote Sens., 57(7), 4485–4489, https://doi.org/10.1109/TGRS.2019.2891338,
913   2019.

914   Lee, J., Kim, J., Song, C. H., Chun, Y., Sohn, B. J., and Holben, B. N.: Characteristics of aerosol types from AERONET
915   sunphotometer measurements, Atmos. Environ., 44, 3110–3117, 2010.

916   Levy, R. C., Leptoukh, G. G., Kahn, R., Zubko, V., Gopalan, A., and Remer, L. A.: A critical look at deriving monthly aerosol
917   optical depth from satellite data, IEEE Transactions on Geoscience and Remote Sensing, 47, 2942–2956,
918   https://doi.org/10.1109/TGRS.2009.2013842, 25, 2009.

919   Logothetis, S.-A., Salamalikis, V. and Kazantzidis, A.: Aerosol classification in Europe, Middle East, North Africa and
920   Arabian Peninsula based on AERONET Version 3, Atmos. Res., 239, https://doi.org/10.1016/j.atmosres.2020.104893, 2020.

921   Logothetis, S.-A., Salamalikis, V. and Kazantzidis, A.: The impact of different aerosol properties and types on direct aerosol
922   radiative   forcing   and   efficiency   using   AERONET   version   3,   Atmos.   Res.,   250,
923   https://doi.org/10.1016/j.atmosres.2020.105343, 2021.

924   Li, J., Carlson, B. E., Dubovik, O. and Lacis, A. A.: Recent trends in aerosol optical properties derived from AERONET
925   measurements, Atmos. Chem. Phys., 14(22), 12271–12289, https://doi.org/10.5194/acp-14-12271-2014, 2014.

926 Mahowald, N., Albani, S., Kok, J. F., Engelstaeder, S., Scanza, R., Ward, D. S., and Flanner, M. G.: The size distribution of
927 desert dust aerosols and its impact on the Earth system, Aeolian Res., 15, 53–71, https://doi.org/10.1016/j.aeolia.2013.09.002,
928 2014.

929 Mielonen, T., Arola, A., Komppula, M., Kukkonen, J., Koskinen, J., de Leeuw, G., and Lehtinen, K.: Comparison of CALIOP
930 level 2 aerosol subtypes to aerosol types derived from AERONET inversion data, Geophys. Res. Lett., 36, L18804,
931 https://doi.org/10.1029/2009gl039609, 2009.

932 Mona, L., Amodeo, A., Pandolfi, M., and Pappalardo, G.: Saharan dust intrusions in the Mediterranean area: Three years of
933 Raman lidar measurements, J. Geophys. Res., 111, D16203, https://doi.org/10.1029/2005JD006569, 2006.

934 Mona, L., Liu, Z., Müller, D., Omar, A., Papayannis, A., Pappalardo, G., Sugimoto, N., and Vaughan, M.: Lidar Measurements
935 for Desert Dust Characterization: An Overview, Adv. Meteorol., 2012, 356265, https://doi.org/10.1155/2012/356265, 2012.

936 Nabat, P., Somot, S., Mallet, M., Chiapello, I., Morcrette, J. J., Solmon, F., Szopa, S., Dulac, F., Collins, W., Ghan, S.,
937 Horowitz, L. W., Lamarque, J. F., Lee, Y. H., Naik, V., Nagashima, T., Shindell, D., and Skeie, R.: A 4-D climatology (1979–
938 2009) of the monthly tropospheric aerosol optical depth distribution over the Mediterranean region from a comparative
939 evaluation and blending of remote sensing and model products, Atmos. Meas. Tech., 6, 1287–1314,
940 https://doi.org/10.5194/amt-6-1287-2013, 2013.

941 Ningombam, S. S., Larson, E. J. L., Dumka, U. C., Estellés, V., Campanelli, M. and Steve, C.: Long-term (1995–2018) aerosol
942 optical depth derived using ground based AERONET and SKYNET measurements from aerosol aged-background sites,
943 Atmos. Pollut. Res., 10(2), 608–620, https://doi.org/10.1016/j.apr.2018.10.008, 2019.

944 Notaro, M., Yu, Y., and Kalashnikova, O. V.: Regime shift in Arabian dust activity, triggered by persistent Fertile Crescent
945 drought, J. Geophys. Res.-Atmos., 120, 10229–10249, https://doi.org/10.1002/2015JD023855, 2015.

946 O'Neill, N. T., Ignatov, A., Holben, B. N., and Eck, T. F.: The lognormal distribution as a reference for reporting aerosol
947 optical depth statistics; Empirical tests using multi-year, multi-site AERONET Sunphotometer data, Geophys. Res. Lett., 27,
948 3333–3336, https://doi.org/10.1029/2000GL011581, 2000.

949 O'Neill, N. T., Dubovik, O., and Eck, T. F.: Modified Ångström coefficient for the characterization of sub-micrometer aerosols,
950 Appl. Optics, 40, 2368–2375, https://doi.org/10.1364/AO.40.002368, 2001.

951 O'Neill, N. T., Eck, T. F., Smirnov, A., Holben, B. N., and Thulasiraman, S.: Spectral discrimination of coarse and fine mode
952 optical depth, J. Geophys. Res., 108, 4559–4573, https://doi.org/10.1029/2002JD002975, 2003.

953 Papadimas, C. D., Hatzianastassiou, N., Mihalopoulos, N., Querol, X., and Vardavas, I.: Spatial and temporal variability in
954 aerosol properties over the Mediterranean basin based on 6- year (2000–2006) MODIS data, J. Geophys. Res., 113, D11205,
955 https://doi.org/10.1029/2007JD009189, 2008.

956 Papayannis, A., Amiridis, V., Mona, L., Tsaknakis, G., Balis, D., Bösenberg, J., Chaikovski, A., De Tomasi, F., Grigorov, I.,
957 Mattis,I., Mitev, V., Muller, D., Nickovic, S., Pérez, C., Pietruczuk, A., Pisani, G., Ravetta, F., Rizi, V., Sicard, M., Trickl, T.,
958 Wiegner, M., Gerding, M., Mamouri, R. E., D'Amico, G., and Pappalardo, G.: Systematic lidar observations of Saharan dust
959 over Europe in the frame of EARLINET (2000–2002), J. Geophys. Res., 113, D10204, https://doi.org/10.1029/2007JD009028,
960 2008.

961 Pan, B., Wang, Y., Hu, J., Lin, Y., Hsieh, J.-S., Logan, T., Feng, X., Jiang, J. H., Yung, Y. L., and Zhang, R.: Impacts of
962 Saharan Dust on Atlantic Regional Climate and Implications for Tropical Cyclones, Journal of Climate, 31, 7621-7644,
963 10.1175/jcli-d-16-0776.1, 2018.

964 Pandey, S. K., Vinoj, V., Landu, K. and Babu, S. S.: Declining pre-monsoon dust loading over South Asia: Signature of a
965 changing regional climate, Sci. Rep., 7(1), 1–10, https://doi.org/10.1038/s41598-017-16338-w, 2017.

966 Pozzer, A., de Meij, A., Yoon, J., Tost, H., Georgoulias, A. K., and Astitha, M.: AOD trends during 2001–2010 from
967 observations and model simulations, Atmos. Chem. Phys., 15, 5521–5535, https://doi.org/10.5194/acp-15-5521-2015, 2015.

968 Proestakis, E., Amiridis, V., Marinou, E., Georgoulias, A. K., Solomos, S., Kazadzis, S., Chimot, J., Che, H., Alexandri, G.,
969 Binietoglou, I., Daskalopoulou, V., Kourtidis, K. A., de Leeuw, G., and van der A, R. J.: Nine-year spatial and temporal
970 evolution of desert dust aerosols over South and East Asia as revealed by CALIOP, Atmos. Chem. Phys., 18, 1337-1362,
971 https://doi.org/10.5194/acp-18-1337-2018, 2018.

972 Prospero, J. M., Ginoux, P., Torres, O., Nicholson, S. E., and Gill, T. E.: Environmental characterization of global sources of
973 atmospheric soil dust identified with the Nimbus 7 Total Ozone Mapping Spectrometer (TOMS) absorbing aerosol product,
974 Rev. Geophys., 40, 2-1–2-31, https://doi.org/10.1029/2000RG000095, 2002.

975 Prospero, J. M. and Lamb, P. J.: African Droughts and Dust Transport to the Caribbean: Climate Change Implications, Science,
976 302, 1024–1027, https://doi.org/10.1126/science.1089915, 2003.

977 Prospero, J. M. and Mayol-Bracero, O. L.: Understanding the transport and impact of African dust on the Caribbean Basin,
978 Bull. Am. Meteorol. Soc., 94(9), 1329–1337, https://doi.org/10.1175/BAMS-D-12-00142.1, 2013.

979 Prospero, J. M., Collard, F. X., Molinie, J., and Jeannot, A.: Characterizing the annual cycle of African dust transport to the
980 Caribbean Basin and South America and its impact on the environment and air quality, Global Biogeochem. Cy., 28, 757–773,
981 https://doi.org/10.1002/2013gb004802, 2014.

982 Rajot, J. L., Formenti, P., Alfaro, S., Desboeufs, K., Chevaillier, S., Chatenet, B., Gaudichet, A., Journet, E., Marticorena, B.,
983 Triquet, S., Maman, A., Mouget, N., and Zakou, A.: AMMA dust experiment: An overview of measurements performed during
984 the dry season special observation period (SOP0) at the Banizoumbou (Niger) supersite, J Geophys Res-Atmos, 113,
985 https://doi.org/10.1029/2008JD009906, 2008.

986 Rashki, A., Kaskaoutis, D. G., Francois, P., Kosmopoulos, P. G. and Legrand, M.: Dust-storm dynamics over Sistan region,
987 Iran: Seasonality,   transport   characteristics   and   affected   areas,   AEOLIAN   Res.,   16,   35–48,
988 https://doi.org/10.1016/j.aeolia.2014.10.003, 2015.

989 Remer, L. A., Kleidman, R. G., Levy, R. C., Kaufman, Y. J., Tanré, D., Mattoo, S., Martins, J. V., Ichoku, C., Koren, I., Yu,
990 H., and Holben, B. N.: Global aerosol climatology from the MODIS satellite sensors, J. Geophys. Res.-Atmos., 113, d14S07,
991 https://doi.org/10.1029/2007JD009661, 2008.

992 Sayer, A. M. and Knobelspiesse, K. D.: How should we aggregate data? Methods accounting for the numerical distributions,
993 with an assessment of aerosol optical depth, Atmos. Chem. Phys., 19, 15023–15048, https://doi.org/10.5194/acp-19-15023-
994 2019, 2019.

995 Schepanski,   K.:   Transport   of   mineral   dust   and   its   impact   on   climate,   Geosciences,   8,   151,
996 https://doi.org/10.3390/geosciences8050151, 2018.

997 Shikwambana, L. and Sivakumar, V.: Global distribution of aerosol optical depth in 2015 using CALIPSO level 3 data, J.
998 Atmos. Solar-Terrestrial Phys., 173, 150–159, https://doi.org/10.1016/j.jastp.2018.04.003, 2018.

999 Shi, L., Zhang, J., Yao, F., Zhang, D. and Guo, H.: Drivers to dust emissions over dust belt from 1980 to 2018 and their
1000 variation in two global warming phases. Sci. Total Environ., 767, 144860, https://doi.org/10.1016/j.scitotenv.2020.144860,
1001 2021.

1002 Song, Q., Zhang, Z., Yu, H., Ginoux, P., and Shen, J.: Global Dust Optical Depth Climatology Derived from CALIOP and
1003 MODIS Aerosol Retrievals on Decadal Time Scales: Regional and Interannual Variability, Atmos. Chem. Phys. Discuss.
1004 [preprint], https://doi.org/10.5194/acp-2021-1, 17 February 2021.

1005 Textor, C., Schulz, M., Guibert, S., Kinne, S., Balkanski, Y., Bauer, S., Berntsen, T., Berglen, T., Boucher, O., Chin, M.,
1006 Dentener, F., Diehl, T., Easter, R., Feichter, H., Fillmore, D., Ghan, S., Ginoux, P., Gong, S., Grini, A., Hendricks, J., Horowitz,
1007 L., Huang, P., Isaksen, I., Iversen, I., Kloster, S., Koch, D., Kirkevåg, A., Kristjansson, J. E., Krol, M., Lauer, A., Lamarque,
1008 J. F., Liu, X., Montanaro, V., Myhre, G., Penner, J., Pitari, G., Reddy, S., Seland, Ø., Stier, P., Takemura, T., and Tie, X.:
1009 Analysis and quantification of the diversities of aerosol life cycles within AeroCom, Atmos. Chem. Phys., 6, 1777–1813,
1010 https://doi.org/10.5194/acp-6-1777-2006, 2006.

1011 Todd, M.C., Washington, R., Martins, J.V., Dubovik, O., Lizcano, G., M'Bainayel, S., Engelstaedter, S.: Mineral dust emission
1012 from the Bodélé Depression nothern Chad, during BoDEx 2005, J. Geophys. Res. Atmos., 112, 1–12,
1013 https://doi.org/10.1029/2006JD007170, 2007.

1014 Torres, O., Bhartia, P. K., Herman, J. R., Sinyuk, A., Ginoux, P., and Holben, B.: A long-term record of aerosol optical depth
1015 from TOMS observations and comparison to AERONET measurements, J. Atmos. Sci., 59, 398–413,
1016 https://doi.org/10.1175/1520- 0469(2002)0592.0.CO;2, 2002.

1017 Tsamalis, C., Chédin, A., Pelon, J., and Capelle, V.: The seasonal vertical distribution of the Saharan Air Layer and its
1018 modulation by the wind, Atmos. Chem. Phys., 13, 11235–11257, https://doi.org/10.5194/acp-13-11235-2013, 2013.

1019 Voss, K. K., and Evan, A. T.: A new satellite-based global climatology of dust aerosol optical depth, Journal of Applied
1020 Meteorology and Climatology, https://doi.org/10.1175/JAMC-D-19-0194.1, 2020.

1021 Washington, R., Todd, M.C., Engelstaedter, S., Mbainayel, S., Mitchell, F.: Dust and the low-level circulation over the Bodélé
1022 Depression, Chad: Observations from BoDEx 2005, J. Geophys. Res. Atmos., 111, 1–15,
1023 https://doi.org/10.1029/2005JD006502, 2006.

1024 Weatherhead, E. C., Reinsel, G. C., Tiao, G. C., Meng, X.-L., Choi, D., Cheang, W.-K., Keller, T., DeLuisi, J., Wuebbles, D.
1025 J., Kerr, J. B., Miller, A. J., Oltmans, S. J., and Frederick, J. E.: Factors affecting the detection of trends: Statistical
1026 considerations and applications to environmental data, J. Geophys. Res., 103(D14), 17149–17161,
1027 https://doi.org/10.1029/98JD00995,1998.

1028 van der Does, M., Knippertz, P., Zschenderlein, P., Harrison, R. G., and Stuut, J. B. W.: The mysterious long-range transport

1029 of giant mineral dust particles, Sci. Adv., 4, eaau2768, https://doi.org/10.1126/sciadv.aau2768, 2018.

1030 Wei, J., Peng, Y., Mahmood, R., Sun, L., and Guo, J.: Intercomparison in spatial distributions and temporal trends derived

1031 from multi-source satellite aerosol products, Atmos. Chem. Phys., 19, 7183–7207, https://doi.org/10.5194/acp-19-7183-2019,

1032 2019a.

1033 Wei, J., Li, Z., Peng, Y., and Sun, L.: MODIS Collection 6.1 aerosol optical depth products over land and ocean: validation

1034 and comparison, Atmos. Environ., 201, 428–440, 2019b.

1035 Xi, X. and Sokolik, I. N.: Dust interannual variability and trend in Central Asia from 2000 to 2014 and their climatic linkages,

1036 J. Geophys. Res., 120, 12175–12197, https://doi.org/10.1002/2015JD024092, 2015.

1037 Xian, P., Klotzbach, P. J., Dunion, J. P., Janiga, M. A., Reid, J. S., Colarco, P. R., and Kipling, Z.: Revisiting the relationship

1038 between Atlantic dust and tropical cyclone activity using aerosol optical depth reanalyses: 2003–2018, Atmos. Chem. Phys.,

1039 20, 15357–15378, https://doi.org/10.5194/acp-20-15357-2020, 2020.

1040 Yoon, J., Burrows, J. P., Vountas, M., von Hoyningen-Huene, W., Chang, D. Y., Richter, A., and Hilboll, A.: Changes in

1041 atmospheric aerosol loading retrieved from space-based measurements during the past decade, Atmos. Chem. Phys., 14, 6881–

1042 6902, https://doi.org/10.5194/acp-14-6881-2014, 2014.

1043 Yu, Y., Notaro, M., Liu, Z., Wang, F., Alkolibi, F., Fadda, E., and Bakhrjy, F.: Climatic controls on the interannual to decadal

1044 variability in Saudi Arabian dust activity: Toward the development of a seasonal dust prediction model, J. Geophys. Res.-

1045 Atmos., 120, 1739–1758, https://doi.org/10.1002/2014JD022611, 2015.

1046 Yu, H., Tan, Q., Chin, M., Remer, L. A., Kahn, R. A., Bian, H., Kim, D., Zhang, Z., Yuan, T., Omar, A. H., Winker, D. M.,

1047 Levy, R. C., Kalashnikova, O., Crepeau, L., Capelle, V., and Chedin, A.: Estimates of African dust deposition along the trans-

1048 Atlantic transit using the decade-long record of aerosol measurements from CALIOP, MODIS, MISR, and IASI, J. Geophys.

1049 Res.-Atmos., 124, 7975–7996, https://doi.org/10.1029/2019JD030574, 2019.

1050 Zender, C. S., Miller, R., and Tegen, I.: Quantifying mineral dust mass budgets: Terminology, constraints, and current

1051 estimates, Eos, Transactions American Geophysical Union, 85, 509–512, https://doi.org/10.1029/2004EO480002, 2004.

Zhang, J. and Reid, J. S.: A decadal regional and global trend analysis of the aerosol optical depth using a data-assimilation grade over-water MODIS and Level 2 MISR aerosol products, Atmos. Chem. Phys., 10, 10949–10963, https://doi.org/10.5194/acp-10-10949-2010, 2010.

Zhang, M., Wang, Y., Ma, Y., Wang, L., Gong, W. and Liu, B.: Spatial distribution and temporal variation of aerosol optical depth and radiative effect in South China and its adjacent area, Atmos. Environ., 188, 120–128, https://doi.org/10.1016/j.atmosenv.2018.06.028, 2018.

Zhao, B., Jiang, J. H., Gu, Y., Diner, D., Worden, J., Liou, K. N., Su, H., Xing, J., Garay, M., and Huang, L.: Decadal-scale trends in regional aerosol particle properties and their linkage to emission changes, Environ. Res. Lett, 12, 054021, https://doi.org/10.1088/1748-9326/aa6cb2, 2017.